Available online at www.sciencedirect.com
SCIENCE DIRECT®
International Journal of Thermal Sciences 44 (2005) 832–850
International Journal of Thermal Sciences
www.elsevier.com/locate/ijts

Convection and radiation effects in hollow, compound optical fibers ☆

J.I. Ramos *

Room I-320-D, ETS Ingenieros Industriales, Universidad de Málaga, Plaza El Ejido, s/n, 29013 Málaga, Spain

Received 4 August 2004; received in revised form 17 February 2005; accepted 22 February 2005

Available online 12 April 2005

Abstract

A coupled model for the study of hollow, compound optical fiber drawing processes that accounts for the heat transfer in the preform and fiber and for the motion of the gases surrounding the preform and fiber by means of two-dimensional equations, employs a net radiative model for the radiative heat exchanges amongst the preform, fiber, irises and furnace walls, and uses asymptotic one-dimensional equations for the geometry, axial velocity component and temperature along the fiber for small Biot numbers is presented. It is shown that the coupled model predicts that radiative heat exchanges are about three times larger than forced convection effects, and free convection is not important. It is also shown that the fiber's geometry, axial velocity and temperature predicted by the coupled model are in remarkable good agreement with those obtained with only the one-dimensional model for hollow, compound fibers using a properly chosen constant Biot number. The results of the one-dimensional model for hollow, compound fibers show that, as the heat transfer losses from the fiber increase, the fiber's dynamic viscosity increases, the fiber exhibits a strong necking phenomenon and the fiber's axial velocity increases rapidly from its value at the die's exit to a constant value downstream and then remains constant. For the boundary conditions considered in this paper, it is shown that the activation energies of the viscosity laws for the inner and outer materials of the hollow, compound fiber do not have very strong effects on the fiber's geometry, axial velocity component and temperature, whereas the fiber's solidification point moves towards the die as the thermal Péclet number is decreased. It is also shown that the pre-exponential factor and activation energy of the dynamic viscosity law do not play a key role in determining the fiber's geometry and temperature for the conditions analyzed in this paper.

Keywords: Optical fibers; Holey fibers; Hollow, compound fibers; Radiative heat transfer; Perturbation methods

1. Introduction

In recent years, holey or microstructured fibers have been developed for optical applications [1]. The cross-section of these fibers contains an array of holes running along the fiber length, and these fibers guide light due to the effective refractive index difference between the solid core and the cladding. These fibers may be made of a single material, such as pure silica, and their effective index contrast can be a strong function of the light guided through the fiber. In addition, depending on the cladding configuration, holey fibers can display anomalous dispersion throughout the visible spectrum.

The presence of air holes in optical holey fibers makes them very useful in applications ranging from nonlinear devices to high-power delivery systems.

Another type of optical holey fibers is the photonic bandgap fiber [2,3] which guides the light by making use of the photonic bandgaps that occur in a periodic structure. Microstructured fibers also include atom-guiding fibers [4] where metal wires are inserted into four electrodes in the fiber and, by running currents along these wires, a magnetic potential can be established. This potential can then guide atoms.

Holey fibers are usually manufactured by drawing a preform in a furnace by conventional fiber-drawing processes. The preform can be made in several ways, including the

☆ A preliminary version of this paper was presented at CHT-04: An ICHMT International Symposium on Advances in Computational Heat Transfer, April 2004, G. de Vahl Davis and E. Leonardi (Eds.), CD-ROM Proceedings, ISBN 1-5670-174-2, Begell House, New York, 2004.

* Tel.: +34 95 2131402; fax: +34 95 2132816.
E-mail address: jirs@lcc.uma.es (J.I. Ramos).

1290-0729/$ – see front matter
doi:10.1016/j.ijthermalsci.2005.02.012

Nomenclature

A	cross-sectional area
B	leading-order axial velocity component, function of x and t
Bi	Biot number
C	function of x and t
Ca	capillary number
C_p	specific heat at constant pressure
D	function of x and t
E	activation energy of the dynamic viscosity law
F	leading-order temperature, function of x and t
Fr	Froude number
g	gravity acceleration
$\bar{h}$	film heat transfer coefficient
h	effective heat transfer coefficient for convection and radiation
k	thermal conductivity
L	axial length
M	Mach number
n	unit outward normal
p	pressure
Pe	thermal Péclet number
Pr	Prandtl number
q	heat flux
Q	energy dissipation rate
r	radial coordinate
R	radius
$\mathbf{R}$	gas constant
Re	Reynolds number
S	pre-exponential factor in the dynamic viscosity law
t	time
T	temperature
x	axial coordinate measured from the furnace top wall or from the furnace exit
u	axial velocity component
v	radial velocity component

Greek symbols

α	thermal diffusivity
β	thermal expansion coefficient
ε	slenderness ratio
ε'	emissivity
μ	dynamic viscosity
ρ	density
σ	Stefan–Boltzmann constant
θ	nondimensional temperature

Subscripts

B	bottom (iris) of furnace
c	convection
ex	gases surrounding the outer annular jet
f	furnace
g	gases surrounding the preform
in	gases enclosed by the inner annular jet
p	preform
pu	spinneret
r	radiation
ref	reference
T	top (iris) of furnace
0	reference value
1	inner annular jet
12	interface between the inner and outer annular jets
2	outer annular jet

Superscript

$*$	dimensional variable

stacking of small capillaries around a solid rod which forms the fiber core, and drilling directly in a solid glass; the latter is frequently used in the manufacture of atom-guiding fibers. In any case, the geometry of the holey fiber can be controlled by acting on the parameters used in the fiber-drawing process such as the temperature of the furnace, the drawing speed, the speed at which the preform is injected or fed into the furnace, etc.

Since the optical properties of microstructured fibers depend strongly on the size and locations of the air holes in the cladding, it is of paramount importance to determine the effects of the drawing conditions on the fiber cross-section. In order to achieve this objective, most theoretical and modelling studies of single hollow fibers have considered a single material, used a slender or long wavelength approximation, and assumed either isothermal flows [5–8] or the heat transfer exchanges between the fibers and the surroundings by means of either a constant Biot number approximation [9] or models for the film heat transfer coefficient as a function of the (local) Reynolds and Prandtl numbers [10]. Radiative heat exchanges have also been considered in these one-dimensional models by correlating these exchanges through a temperature-dependent Biot number. In addition, these one-dimensional models have frequently been derived by means of asymptotic expansions in the slenderness ratio and are only valid for small Biot numbers, have not considered the preform, and have not accounted in a detailed manner for the effects of the radiation and convective flow effects of the gases surrounding the fiber on its dynamics and solidification. Moreover, most of these models employ a constant viscosity and consider Newtonian fluids with either a constant dynamic viscosity [5–8] or a viscosity law of the Arrhenius type [10].

Multidimensional models of optical fiber drawing processes include that of Lee and Jaluria [11] who considered the two-dimensional free-surface flow of fused silica with

a *prescribed necking shape* and variable flow properties, accounted for the radiative transport between the preform, the furnace and the (top and bottom) irises by assuming diffusive, spectral surfaces, neglected the motion of the gases surrounding the preform, included viscous dissipation, and used a stream function-vorticity formulation to determine the temperature in the silica fiber. This formulation is rather complete; however, the use of a prescribed preform shape limits seriously the validity of their model because this shape should really be a result of the overall computation of optical fiber processes, e.g., heating of the preform, and should not be prescribed *à priori*. Other two-dimensional studies of optical fiber drawing processes include those of Yin and Jaluria [12] which has analogous limitations to those of Lee and Jaluria [11], and Rosenberg et al. [13] and Papamichael and Miaoulis [14] who used a von Kárman–Pohlhausen technique to determine the temperature profiles in thick fibers.

Reeve and Mescher [15] have shown experimentally that the air flow adjacent to a polymer optical fiber may be laminar, oscillatory or chaotic, depending on the thermal boundary conditions imposed at the furnace wall and irises, and that, in the chaotic regime, the drawn fiber varies in diameter 2.5 to 10 times more than that measured under laminar heating conditions. Reeve et al. [16] studied the heating of polymer preforms by means of a two-dimensional formulation for the gases in the furnace which accounted for the radiative heat exchanges between the preform, the furnace and the irises, and which assumed isothermal preforms and did not consider the necking of the preform and the fiber.

In this paper, we study the fluid dynamics and heat transfer processes that occur in the manufacture of a single hollow, compound fiber by accounting for convective and radiative heat exchanges between the furnace walls and the preform and fiber, by means of a coupled model; we also study the cooling of the fiber below the heating region or furnace by means of an asymptotic one-dimensional model. The coupled model of hollow, compound fiber drawing presented here is a hybrid analytical–numerical one in that numerical methods are used to determine the radiative heat exchanges between the furnace walls and the preform and fiber, the motion of the gases surrounding the fiber, and conductive heat transfer in the preform, whereas an asymptotic method is used to derive one-dimensional equations for the fiber's geometry and axial velocity component. For small Biot numbers, the temperature along the fiber is also determined asymptotically from the solution of an (asymptotic) one-dimensional equation which includes conduction along the fiber and heat exchanges with the surroundings. When the Biot number is on the order of or larger than one, the temperature in the fiber is two-dimensional with a velocity field which may be approximated by that obtained from a slender or long wavelength theory.

The one-dimensional model presented here can also be used to study fiber spinning processes such as those occurring in the manufacture of glass and textile fibers, i.e., melt spinning processes, where there is no preform. In addition, this model provides a one-dimensional set of equations for the hollow, compound fiber geometry, axial velocity component and temperature at low Biot numbers, which reduces to that for annular or holey fibers if the two materials of the compound jet are identical. Under isothermal conditions, this one-dimensional model reduces to that developed by the author for one-dimensional, hollow, compound fibers [6].

Our objective in this paper is two-fold. First, a coupled model for the study of hollow, compound optical fiber drawing processes that accounts for the heat transfer in the preform and for the motion of the gases surrounding the preform and fiber by means of two-dimensional equations, employs a net radiative model for the radiative heat exchanges amongst the preform, fiber, irises and furnace walls, and uses asymptotic one-dimensional equations for the geometry, axial velocity component and temperature along the fiber for small Biot numbers is presented. The results of this model are then used to determine the magnitude of the radiative and convective heat exchanges and the local Biot numbers along the hollow, compound fiber. Second, calculations are performed with only the asymptotic one-dimensional equations for the hollow, compound fiber's geometry, axial velocity component and temperature using a constant Biot number, and the results of these calculations are compared with those of the coupled model, in order to determine whether or not the one-dimensional model with a constant Biot number approximation provides results in accord with those of the coupled model which is much more complex and requires longer computational times than the solution of the one-dimensional equations for the compound fiber's geometry, axial velocity component and temperature.

The paper has been organized as follows. In Section 2, the governing equations for the hollow, compound preform and fiber and for the gases that surround the preform and fiber are presented. In Section 2.1, it is assumed that the preform is injected or fed into the furnace at constant axial velocity and behaves as a solid material until it reaches its melting temperature due to the radiative heat exchanges with the furnace walls and the convective heat transfer with the gases that surround it. Section 2.2 contains a summary of an asymptotic analysis of slender, hollow, compound fibers at low Reynolds numbers that accounts for capillary and gravitational effects and pressure differences across the fiber. For small Biot numbers, an asymptotic study of the energy equation for the fiber is also presented; this analysis yields a one-dimensional energy equation along the fiber. In Sections 2.3 and 2.4, the equations governing the dynamics of the gases surrounding the fiber and the radiative heat exchanges between the preform, fiber and furnace, respectively, are presented, while, in Section 3, the numerical methodology used to solve the governing equations for the preform, fiber and gases surrounding the fiber is described in some detail. Section 4 presents some sample results to illustrate the heating of the preform and fiber in the furnace (in Section 4.1), and the cooling of hollow, compound optical fibers (in Section 4.2) that have a Newtonian rheology.

2. Formulation

Fig. 1 illustrates the different regions during the drawing of optical fibers. These regions are referred to as 1, 2 and 3 and correspond to neck-down, cooling and coating, respectively. In the neck-down region, a preform is fed into a furnace where the heating of the preform by convection and radiation causes it to melt, while the pulling speed causes it to stretch and accelerate. The fiber exiting the neck-down region is cooled and its diameter is controlled in the cooling region. The cooled fiber then passes trough a coating cup, a coating concentricity monitor, coating curing and a diameter monitor. The cooled and coated fiber is then collected in a drum or spinneret.

A schematic of the neck-down region is presented in Fig. 2 which illustrates the preform, the top and bottom irises and the furnace where the preform is heated. Owing to the pulling of the fiber and the radiative heat exchanges between the preform and the furnace, the fluid dynamics of the preform and fiber in the neck-down region is an extremely complex problem since there is melting and the transition from the preform to the fiber is a free-surface problem where the location of the free surface is coupled to the fluid dynamics and heat transfer equations. It is for this reason that most of the two-dimensional studies concerning the drawing of optical fibers have specified the shape of the preform and fiber, e.g., [11,12], and considered only the fluid dynamics of the preform. In this paper, the necking of the preform has been modelled as indicated in Fig. 3 as follows. We assume that the axisymmetric preform preserves its diameter until, owing to radiative and convective heat exchanges in the neck-down region or furnace, its cross-sectional averaged temperature reaches the melting temperature; this region corresponds to $0 \leqslant x \leqslant L_p$ in Fig. 3. For $L_p \leqslant x \leqslant L_f$ and provided that $R_p \ll L_f - L_p$, we assume that the fiber can be analyzed asymptotically by means of perturbation methods based on the slenderness ratio. Therefore, in the neck-down region, we use a hybrid coupled model based on two-dimensional equations for the axisymmetric preform and one-dimensional equations for the fiber. This coupled model is obviously an approximation to the true geometry of the preform and fiber in the neck-down region (cf. Fig. 2) which has the advantage that its analysis is relatively simple since the preform is assumed to be nondeformable until it reaches the melting temperature, while the shape of the fiber is determined from one-dimensional equations. This simplicity allows us to consider in great detail the convective motions in the gases surrounding the preform and fiber as well as the radiative heat exchanges in the furnace. Moreover, as stated in the Introduction, the one-dimensional model for the fiber is also

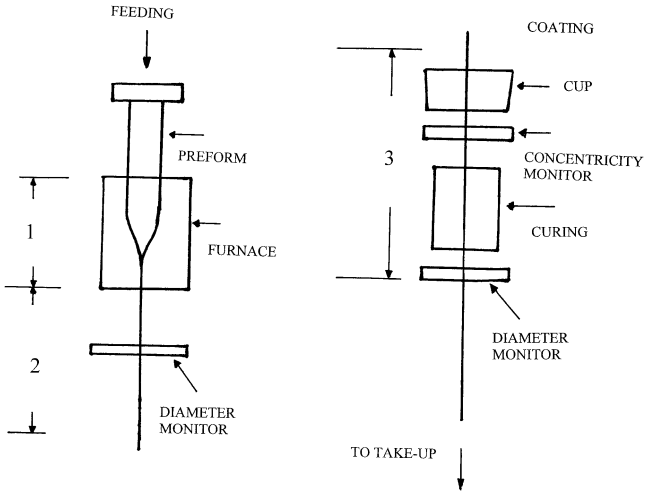

Fig. 1. Schematic showing the different regions in the drawing of optical fibers. (Neck-down or heating region: 1; cooling region: 2; coating region: 3.)

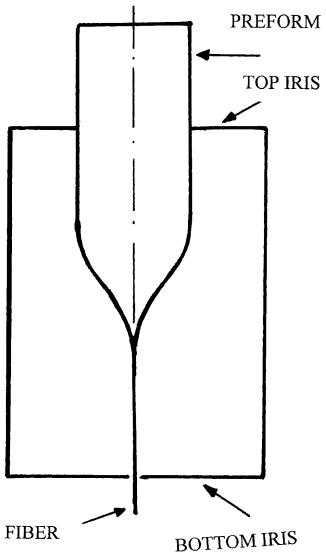

Fig. 2. Schematic of the furnace illustrating the neck-down or heating region, preform and fiber.

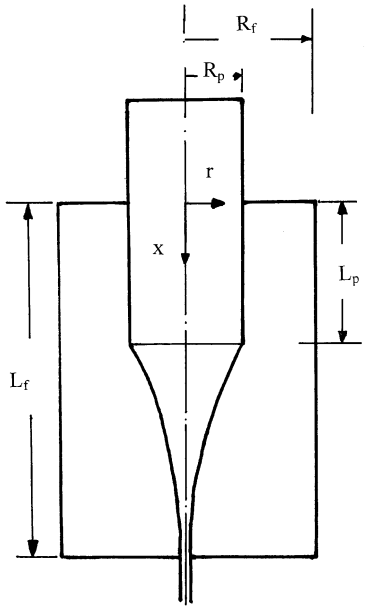

Fig. 3. Schematic of the model used for the neck-down or heating region.

valid to study the cooling of the fiber in the cooling region (cf. Fig. 1).

We, thus, consider a cylindrical furnace of radius R_f and length L_f (Fig. 3). On the top wall of this furnace, i.e., $x = 0$, a hollow, compound preform consisting of an inner material (subscript 1) of inner and outer radii equal to $R_1(0,t)$ and $R(0,t)$, respectively, surrounded by an outer material (subscript 2) of inner and outer radii equal to $R(0,t)$ and $R_2(0,t)$, respectively, at temperatures equal to $T_1(0,r,t)$ and $T_2(x,0,t)$ smaller than the melting temperatures of these materials, is pushed in the vertical x-direction into the furnace (cf. Fig. 4). Owing to the radiative and convective heat transfer exchanges between the furnace walls and the hollow, compound preform, the fiber's materials reach their melting temperatures and a hollow, compound jet is obtained. The temperatures of the furnace vertical wall, i.e., $r = R_f$, and top and bottom irises located at $x = 0$ and $x = L_f$, respectively, are selected so that the hollow, compound fiber melts before reaching the furnace bottom wall, and the melted fiber is pulled down and made to pass through the cooling and coating regions before it is collected downstream at the spinneret at an axial velocity equal to $u_{\mathrm{pu}} > u_p$, where u_p is the axial velocity component at which the preform is introduced into the furnace. Let L_p be the axial distance from the furnace's top wall to the location where the preform melts, i.e., the axial location at which the cross-sectional averaged temperature is identical to the melting temperature, and assume that the preform behaves as a rigid solid material until the melting temperature is reached. Assume also that the melting temperatures of the two materials that compose the hollow, compound preform are very similar, and $\max R_2(0,t) \ll L_f - L_p$ and $\max R_2(0,t) \ll R_f$ so that the hollow, compound fiber is slender and its diameter is much smaller than the furnace diameter, and that $T_1(0,r,t)$ and $T_2(x,0,t)$ do not differ significantly from each other.

Under these conditions, the fluid dynamics of the hollow, compound fiber, i.e., $L_p \leqslant x \leqslant L_f$, may be analyzed by using a slender flow or long wave length approximation from $x = L_p$ to L_f in the axial direction, and from $R_1(x,t)$ to $R_2(x,t)$ in the radial one, while the preform has a constant axial velocity equal to u_p until it reaches the melting temperature at $x = L_p$ which may be a function of time. If the gases surrounding the preform are not participating, radiative heat exchanges occur between the furnace walls and the preform and the hollow, compound fiber. In addition, the difference between the temperature of the vertical, top and bottom walls of the furnace, and the temperature and velocity of the fiber introduce both forced and free convection effects that may result in substantial heat exchanges with the fiber and, therefore, affect its fluid dynamics.

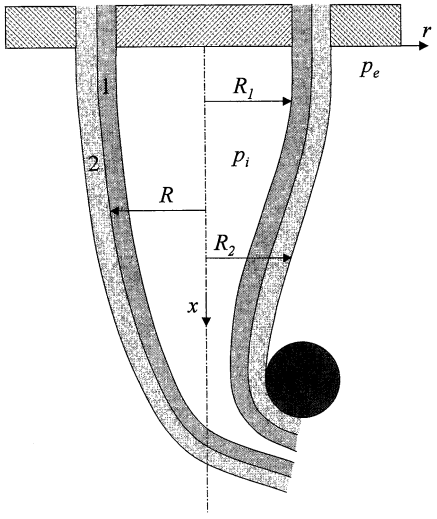

Fig. 4. Schematic of the hollow, compound fiber geometry.

2.1. Governing equations for the preform

In order to analyze the fluid dynamics and the convective and radiative heat transfer phenomena in the preform and the hollow, compound fiber and in the gases that surround the preform and fiber, we shall assume that $R_1(x,t)$, $R(x,t)$ and $R_2(x,t)$ are only functions of time for $0 \leqslant x \leqslant L_p(t)$, i.e., the preform is a hollow cylinder, the preform moves with axial velocity $u_p(t)$ and enters into the furnace at temperatures equal to $T_1(0,r,t)$ and $T_2(0,r,t)$. Under these conditions, the governing equations for the temperature in the two materials that compose the preform can be written as

$$\rho_i C_{pi}\left(\frac{\partial T_i}{\partial t} + u_f \frac{\partial T_i}{\partial x}\right) = k_i \frac{\partial^2 T_i}{\partial x^2} + \frac{k_i}{r}\frac{\partial}{\partial r}\left(r\frac{\partial T_i}{\partial r}\right), \quad i = 1,2 \tag{1}$$

where ρ, C_p and k denote the density, specific heat at constant pressure and thermal conductivity, and are assumed constant. These equations are valid for $0 \leqslant x \leqslant L_p$. At $x = 0$, the temperatures of the two materials is known, and, at $x = L_p$, the temperatures are equal to their melting values which are assumed to be nearly the same for the two materials.

The gases enclosed by the inner surface of the preform are assumed to be dynamically passive and, in this study, we apply the following boundary conditions in the radial direction, for $0 \leqslant x \leqslant L_p$

$$k_1 \frac{\partial T_1}{\partial r}(x, R_1, t) = q_1, \quad T_1(x, R_1, t) = T_g(x, R_1, t) \tag{2}$$

$$k_1 \frac{\partial T_1}{\partial r}(x, R, t) = k_2 \frac{\partial T_2}{\partial r}(x, R, t)$$

$$T_1(x, R, t) = T_2(x, R, t) \tag{3}$$

$$-k_2 \frac{\partial T_2}{\partial r}(x, R_2, t) = q_2, \quad T_2(x, R_2, t) = T_g(x, R_2, t) \tag{4}$$

which reflect the facts that there is heat transfer between the preform and the gases that it encloses, both the temperature and the heat flux at the interface between the two materials that compose the fiber are continuous, and the heat flux and temperature at the preform's outer surface

are continuous and equal to those of the gases surrounding the preform. The heat flux q_2 accounts for convection in the gases surrounding the fiber and radiative heat exchanges with the furnace walls, and may be written as $q_2 = q_c + q_r$ where $q_c = -k_g \frac{\partial T_g}{\partial r}(x, R_2, t)$, the subscript g denotes the gases surrounding the cylindrical preform and q_r will be determined below. A similar comment applies to q_1. Note that q_2 can also be written as $q_2 = \bar{h}_p(T_2(x, R_2, t) - T_{ex}) + \sigma\varepsilon'_p(T_2^4(x, R_2, t) - T_{ex}^4) = h_p(T_2(x, R_2, t) - T_{ex})$ where $h_p \equiv \bar{h}_p + \sigma\varepsilon'_p(T_2^2(x, R_2, t) + T_{ex}^2)(T_2(x, R_2, t) + T_{ex})$, where $\bar{h}_p$ denotes the film heat transfer coefficient at the outer surface of the perform and is a function of the Reynolds and Prandtl numbers, σ is the Stefan–Boltzmann constant, ε'_p is the emissivity of the preform's outer surface, T_{ex} is a reference temperature of the gases surrounding the preform and h_p is an effective film transfer coefficient that, therefore, depends on the Reynolds and Prandtl numbers and the temperatures of the gases that surround the preform and the temperature at the preform's outer surface.

It must be pointed out that there is a mathematical incompatibility between the thermal boundary conditions in the radial direction considered above and the condition that melting occurs at $x = L_p$. In addition, the latent heat of melting has been neglected. A similar approximation will also be used when analyzing the fluid dynamics of the hollow, compound fiber where latent heat effects will be disregarded while the fiber solidification is assumed to occur due to a decrease in temperature that causes an exponential increase in the dynamic viscosity of the two flowing materials that compose the hollow, compound fiber.

2.2. Governing equations for the hollow, compound fiber

Once the preform reaches its melting temperature at $x = L_p(t)$, the materials that compose it flow under the action of gravity and pulling from the spinneret, and a hollow, compound jet is formed. This jet passes through the cooling and coating regions (cf. Fig. 1) before it is collected in a drum or spinneret. The hollow, compound fibers/jets considered in this study are assumed to be incompressible, Newtonian and axisymmetric with a dynamic viscosity that increases in an exponential manner as the temperature decreases, and with constant density, specific heats and thermal conductivity. The governing equations for the two materials of the hollow, compound fiber can be written as (for $L_p \leqslant x \leqslant L_f$ in the neck-down region and for $x_1 \leqslant x \leqslant x_2$, where x_1 and x_2 denote the exit of the furnace and the exit of the cooling region, respectively)

$$\frac{\partial u_i}{\partial x} + \frac{1}{r}\frac{\partial}{\partial r}(r v_i) = 0 \tag{5}$$

$$\rho_i \frac{Du_i}{Dt} = -\frac{\partial p_i}{\partial x} + \frac{\partial}{\partial z}\left(2\mu_i \frac{\partial u_i}{\partial x}\right) + \frac{1}{r}\frac{\partial}{\partial r}\left(\mu_i r\left(\frac{\partial u_i}{\partial r} + \frac{\partial v_i}{\partial x}\right)\right) + \rho_i g \tag{6}$$

$$\rho_i \frac{Dv_i}{Dt} = -\frac{\partial p_i}{\partial r} + \frac{1}{r}\frac{\partial}{\partial r}\left(2\mu_i r \frac{\partial v_i}{\partial r}\right) + \frac{\partial}{\partial z}\left(\mu_i\left(\frac{\partial u_i}{\partial r} + \frac{\partial v_i}{\partial x}\right)\right) - \frac{2\mu_i v}{r^2} \tag{7}$$

$$\rho_i C_{pi} \frac{DT_i}{Dt} = k_i \frac{\partial^2 T_i}{\partial x^2} + \frac{k_i}{r}\frac{\partial}{\partial r}\left(r\frac{\partial T_i}{\partial r}\right) + Q_i \tag{8}$$

where t is the time, x and r are axial and radial coordinates, respectively, u and v are the axial and radial velocity components, respectively, p and T are the pressure and temperature, respectively, ρ, μ and k are the density, dynamic viscosity and thermal conductivity, respectively, $i = 1, 2$ denote the inner and outer materials, respectively, characterized by $R_1(x, t) \leqslant r \leqslant R(x, t)$ and $R(x, t) \leqslant r \leqslant R_2(x, t)$, respectively, R_1 denotes the radius of the inner material's inner interface, R is the interface between the inner and outer materials, and R_2 is the radius of the outer material's outer interface (cf. Fig. 4), g is the gravitational acceleration, $\frac{DU}{Dt} = \frac{\partial U}{\partial t} + u\frac{\partial U}{\partial x} + v\frac{\partial U}{\partial r}$, C_p and k are the specific heat at constant pressure and the thermal conductivity, respectively, and the energy dissipation rate, Q, is

$$Q = 2\mu\left(\left(\frac{\partial u}{\partial x}\right)^2 + \left(\frac{\partial v}{\partial r}\right)^2 + \left(\frac{v}{r}\right)^2 + \left(\frac{\partial u}{\partial r} + \frac{1}{2}\frac{\partial v}{\partial x}\right)^2\right) \tag{9}$$

Eqs. (5)–(8) are subject to the following boundary conditions. The gases enclosed by the inner material and those surrounding the outer material are assumed to be dynamically passive because they have smaller densities and dynamic viscosities than those of the compound fiber's inner and outer materials, respectively, and the three interfaces are material ones. At the interfaces, the shear stress must be continuous, whereas the jump in normal stresses is balanced out by surface tension. The kinematic and dynamic boundary conditions at the three interfaces can be written as

$$v_i\big(x, R_i(x, t), t\big) = \frac{\partial R_i}{\partial t} + u_i\big(x, R_i(x, t), t\big)\frac{\partial R_i}{\partial x}, \quad i = 1, 2 \tag{10}$$

$$v_i\big(x, R(x, t), t\big) = \frac{\partial R}{\partial t} + u_i\big(x, R(x, t), t\big)\frac{\partial R}{\partial x}, \quad i = 1, 2 \tag{11}$$

$$2\mu_i\left(\frac{\partial v_i}{\partial r} - \frac{\partial u_i}{\partial x}\right)\frac{\partial R_i}{\partial x} + \mu_i\left(\frac{\partial u_i}{\partial r} + \frac{\partial v_i}{\partial x}\right)\left(1 - \left(\frac{\partial R_i}{\partial x}\right)^2\right) = 0 \quad i = 1, 2 \tag{12}$$

$$2\mu_2\left(\frac{\partial v_2}{\partial r} - \frac{\partial u_2}{\partial x}\right)\frac{\partial R}{\partial x} + \mu_2\left(\frac{\partial u_2}{\partial r} + \frac{\partial v_2}{\partial x}\right)\left(1 - \left(\frac{\partial R}{\partial x}\right)^2\right) = 2\mu_1\left(\frac{\partial v_1}{\partial r} - \frac{\partial u_1}{\partial x}\right)\frac{\partial R}{\partial x}$$

$$+\mu_1\left(\frac{\partial u_1}{\partial r}+\frac{\partial v_1}{\partial x}\right)\left(1-\left(\frac{\partial R}{\partial x}\right)^2\right), \quad \text{at } r=R \tag{13}$$

$$2\mu_1\frac{\partial u_1}{\partial x}\left(\frac{\partial R_1}{\partial x}\right)^2+2\mu_1\frac{\partial v_1}{\partial r}-2\mu_1\left(\frac{\partial u_1}{\partial r}+\frac{\partial v_1}{\partial x}\right)\frac{\partial R_1}{\partial x}+(p_{\text{in}}-p_1)\left(1+\left(\frac{\partial R}{\partial x}\right)^2\right)=\sigma_1 J_1, \quad \text{at } r=R_1 \tag{14}$$

$$2\mu_2\frac{\partial u_2}{\partial x}\left(\frac{\partial R_2}{\partial x}\right)^2+2\mu_2\frac{\partial v_2}{\partial r}-2\mu_2\left(\frac{\partial u_2}{\partial r}+\frac{\partial v_2}{\partial x}\right)\frac{\partial R_2}{\partial x}+(p_{\text{ex}}-p_2)\left(1+\left(\frac{\partial R_2}{\partial x}\right)^2\right)=\sigma_2 J_2, \quad \text{at } r=R_2 \tag{15}$$

$$2\mu_2\frac{\partial u_2}{\partial x}\left(\frac{\partial R}{\partial x}\right)^2+2\mu_2\frac{\partial v_2}{\partial r}-2\mu_2\left(\frac{\partial u_2}{\partial r}+\frac{\partial v_2}{\partial x}\right)\frac{\partial R}{\partial x}+(p_1-p_2)\left(1+\left(\frac{\partial R}{\partial x}\right)^2\right)=2\mu_1\frac{\partial u_1}{\partial x}\left(\frac{\partial R}{\partial x}\right)^2+2\mu_1\frac{\partial v_1}{\partial r}-2\mu_1\left(\frac{\partial u_1}{\partial r}+\frac{\partial v_1}{\partial x}\right)\frac{\partial R}{\partial x}+\sigma_{12}J, \quad \text{at } r=R \tag{16}$$

where σ_1 is the surface tension at the inner interface of the inner material, σ_2 is the surface tension at the outer material's outer interface, σ_{12} is the surface tension at the interface between the two materials that form the hollow, compound fiber, p_{in} is the pressure of the gases enclosed by the inner material, p_{ex} is the pressure of the gases surrounding the fiber's outer material, and

$$J_i=\frac{\phi_i}{R_i}-\frac{1}{\phi_i}\frac{\partial^2 R_i}{\partial x^2}, \quad \phi_i=\left(1+\left(\frac{\partial R_i}{\partial x}\right)^2\right)^{1/2} \quad i=1,2 \tag{17}$$

$$J=\frac{\phi}{R}-\frac{1}{\phi}\frac{\partial^2 R}{\partial x^2}, \quad \phi=\left(1+\left(\frac{\partial R}{\partial x}\right)^2\right)^{1/2} \tag{18}$$

In general, both p_{in} and p_{ex} are space and time dependent, but, at the low Mach numbers considered in this study, they may be assumed to be constant with an error on $\mathrm{O}(M^2)$, where M denotes the Mach number.

The dynamic viscosities employed in this study may be written as

$$\mu_i=S_i e^{E_i(T_{\text{ref}}-T)} \tag{19}$$

where $i=1, 2$, T_{ref} is a (constant) reference temperature, and $S_i>0$ and $E_i\geqslant 0$ are constant with the dimensions of dynamic viscosity and inverse of temperature, respectively. These viscosity laws imply that the dynamic viscosity increases exponentially with temperature for $E_i>0$ and $T<T_{\text{ref}}$, and can be interpreted as a linearization or approximation to the exponent of the Arrhenius law; constant viscosity corresponds to $E_i=0$. In the sequel, we shall refer to S_i and E_i as the pre-exponential factor and activation energy of the dynamic viscosity law, respectively.

The thermal boundary conditions are as follows

$$T_1(x,R,t)=T_2(x,R,t) \tag{20}$$

$$k_1\frac{\partial T_1}{\partial n}(x,R,t)=k_2\frac{\partial T_2}{\partial n}(x,R,t) \tag{21}$$

$$-k_1\frac{\partial T_1}{\partial n_1}(x,R_1,t)=h_1\big(T_{\text{in}}-T_1(x,R_1,t)\big)$$

$$T_1(x,R_1,t)=T_g(x,R_1,t) \tag{22}$$

$$-k_2\frac{\partial T_2}{\partial n_2}(x,R_2,t)=h_2\big(T_2(x,R_2,t)-T_{\text{ex}}\big)$$

$$T_2(x,R_2,t)=T_g(x,R_2,t) \tag{23}$$

where n_1, n and n_2 denote the normal coordinates to the interfaces $r=R_1$, R and R_2, respectively, and h_1 and h_2 denote the heat transfer coefficients that include convection and radiation. These coefficients are, in general, functions of the Reynolds and Prandtl numbers and the temperature as discussed previously in Section 2.1, and include the effects of convection and radiation heat transfer; in fact, they have a similar expression to that for the boundary conditions at the outer surface of the preform, and, therefore, $-k_2\frac{\partial T_2}{\partial n_2}(x,R_2,t)=h_2(T_2(x,R_2,t)-T_{\text{ex}})=-k_g\frac{\partial T_g}{\partial n_2}(x,R_2,t)+q_r$.

Nondimensionalization of the radial and axial coordinates with respect to R_0 and $L=L_f-\overline{L}_p$ in the furnace or $L=x_2-x_1$ in the cooling region, where R_0 is a characteristic radius, $\overline{L}_p$ denotes a constant reference value characteristic of the length of the preform, the axial and radial velocity components with respect to u_0 and $v_0=R_0u_0/L$, respectively, p with respect to μ_0u_0/L, densities and dynamic viscosities with respect to ρ_0 and μ_0, respectively, and temperature as $\theta=(T-T_0)/\Delta T$, where quantities with the subscript 0 and ΔT are constant values, one obtains the following system of governing equations

$$\frac{\partial u_i}{\partial x}+\frac{1}{r}\frac{\partial}{\partial r}(rv_i)=0 \tag{24}$$

$$\varepsilon\,Re\,\rho_i\frac{Du_i}{Dt}=-\varepsilon^2\frac{\partial p_i}{\partial x}+\frac{\partial}{\partial z}\left(2\varepsilon^2\mu_i\frac{\partial u_i}{\partial x}\right)+\frac{1}{r}\frac{\partial}{\partial r}\left(\mu_i r\left(\frac{\partial u_i}{\partial r}+\varepsilon^2\frac{\partial v_i}{\partial x}\right)\right)+\frac{Re}{Fr}\rho_i \tag{25}$$

$$\varepsilon\,Re\,\rho_i\frac{Dv_i}{Dt}=-\frac{\partial p_i}{\partial r}+\frac{1}{r}\frac{\partial}{\partial r}\left(2\mu_i r\frac{\partial v_i}{\partial r}\right)+\frac{\partial}{\partial z}\left(\mu_i\left(\frac{\partial u_i}{\partial r}+\varepsilon^2\frac{\partial v_i}{\partial x}\right)\right)-\frac{2\mu_i v}{r^2} \tag{26}$$

$$\varepsilon\,Re\,Pr\frac{D\theta_i}{Dt}=\alpha_i\left(\varepsilon^2\frac{\partial^2\theta_i}{\partial x^2}+\frac{1}{r}\frac{\partial}{\partial r}\left(r\frac{\partial\theta_i}{\partial r}\right)\right)+\frac{\nu_i M^2 Pr}{C_{pi}}\overline{Q}_i \tag{27}$$

where, for the sake of conciseness, the same symbols have been used for dimensional and dimensionless quantities, $\alpha_i=k_i/\rho_i C_{pi}$, μ_i, ρ_i, k_i and C_{pi} have been nondimensionalized with respect to μ_0, ρ_0, k_0 and C_{p0}, respectively, $M^2=$

$u_0^2/C_{p0}\Delta T$, $\varepsilon = R_0/L$, $Pr = \mu_0 C_{p0}/k_0$ is the Prandtl number, $Re = \rho_0 u_0 R_0/\mu_0$ is the Reynolds number, $Fr = u_0^2/gR_0$ is the Froude number, and

$$\overline{Q} = 2\varepsilon^2\left(\left(\frac{\partial u}{\partial x}\right)^2 + \left(\frac{\partial v}{\partial r}\right)^2 + \left(\frac{v}{r}\right)^2\right) + \left(\frac{\partial u}{\partial r} + \varepsilon^2\frac{\partial v}{\partial x}\right)^2 \tag{28}$$

subject to

$$v_i\big(x, R_i(x,t), t\big) = \frac{\partial R_i}{\partial t} + u_i\big(x, R_i(x,t), t\big)\frac{\partial R_i}{\partial x}, \quad i = 1,2 \tag{29}$$

$$v_i\big(x, R(x,t), t\big) = \frac{\partial R}{\partial t} + u_i\big(x, R(x,t), t\big)\frac{\partial R}{\partial x}, \quad i = 1,2 \tag{30}$$

$$2\varepsilon^2\left(\frac{\partial v_i}{\partial r} - \frac{\partial u_i}{\partial x}\right)\frac{\partial R_i}{\partial x} + \mu_i\left(\frac{\partial u_i}{\partial r} + \varepsilon^2\frac{\partial v_i}{\partial x}\right) \times\left(1 - \varepsilon^2\left(\frac{\partial R_i}{\partial x}\right)^2\right) = 0, \quad i = 1,2 \tag{31}$$

$$2\varepsilon^2\mu_2\left(\frac{\partial v_2}{\partial r} - \frac{\partial u_2}{\partial x}\right)\frac{\partial R}{\partial x} + \mu_2\left(\frac{\partial u_2}{\partial r} + \varepsilon^2\frac{\partial v_2}{\partial x}\right)\left(1 - \varepsilon^2\left(\frac{\partial R}{\partial x}\right)^2\right) = 2\varepsilon^2\mu_1\left(\frac{\partial v_1}{\partial r} - \frac{\partial u_1}{\partial x}\right)\frac{\partial R}{\partial x} + \mu_1\left(\frac{\partial u_1}{\partial r} + \varepsilon^2\frac{\partial v_1}{\partial x}\right) \times\left(1 - \varepsilon^2\left(\frac{\partial R}{\partial x}\right)^2\right), \quad \text{at } r = R \tag{32}$$

$$2\varepsilon^2\mu_1\frac{\partial u_1}{\partial x}\left(\frac{\partial R_1}{\partial x}\right)^2 + 2\mu_1\frac{\partial v_1}{\partial r} - 2\mu_1\left(\frac{\partial u_1}{\partial r} + \varepsilon^2\frac{\partial v_1}{\partial x}\right)\frac{\partial R_1}{\partial x} + (p_i - p_1)\left(1 + \varepsilon^2\left(\frac{\partial R}{\partial x}\right)^2\right) = \frac{1}{\varepsilon Ca_1}J_1, \quad \text{at } r = R_1 \tag{33}$$

$$2\varepsilon^2\mu_2\frac{\partial u_2}{\partial x}\left(\frac{\partial R_2}{\partial x}\right)^2 + 2\mu_2\frac{\partial v_2}{\partial r} - 2\mu_2\left(\frac{\partial u_2}{\partial r} + \varepsilon^2\frac{\partial v_2}{\partial x}\right)\frac{\partial R_2}{\partial x} + (p_e - p_2)\left(1 + \varepsilon^2\left(\frac{\partial R_2}{\partial x}\right)^2\right) = \frac{1}{\varepsilon Ca_2}J_2, \quad \text{at } r = R_2 \tag{34}$$

$$2\mu_2\frac{\partial u_2}{\partial x}\left(\frac{\partial R}{\partial x}\right)^2 + 2\mu_2\frac{\partial v_2}{\partial r} - 2\mu_2\left(\frac{\partial u_2}{\partial r} + \varepsilon^2\frac{\partial v_2}{\partial x}\right)\frac{\partial R}{\partial x} + (p_1 - p_2)\left(1 + \varepsilon^2\left(\frac{\partial R}{\partial x}\right)^2\right) = 2\varepsilon^2\mu_1\frac{\partial u_1}{\partial x}\left(\frac{\partial R}{\partial x}\right)^2 + 2\mu_1\frac{\partial v_1}{\partial r} - 2\mu_1\left(\frac{\partial u_1}{\partial r} + \varepsilon^2\frac{\partial v_1}{\partial x}\right)\frac{\partial R}{\partial x} + \frac{1}{\varepsilon Ca}J, \quad \text{at } r = R \tag{35}$$

Table 1
Relations between dimensional and dimensionless variables, and nondimensional parameters

Dimensional variable	Dimensionless variable	Dimensionless parameter
x^*	$x = x^*/L^*$	$\varepsilon = R_0^*/L^*$
r^*	$r = r^*/R_0^*$	$M^2 = u_0^{*2}/C_{p0}^*\Delta T^*$
u^*	$u = u^*/u_0^*$	$Re = \rho_0^* u_0^*/\mu_0^*$
v^*	$v = v^*/(\varepsilon u_0^*)$	$Fr = u_0^{*2}/g^* R_0^*$
T^*	$\theta = (T^* - T_0^*)/\Delta T^*$	$Pr = \mu_0^* C_{p0}^*/k_0^*$
p^*	$p = \mu_0^* u_0^*/L^*$	$Ca = \mu_0^* u_0^*/\sigma_0^*$
ρ^*	$\rho = \rho^*/\rho_0^*$	$Bi = h_0^* R_0^*/k_0^*$
μ^*	$\mu = \mu^*/\mu_0^*$	$Pe = Re\,Pr$
k^*	$k = k^*/k_0^*$	
C_p^*	$C_p = C_p^*/C_{p0}^*$	
h^*	$h = h^*/h_0^*$	

$$\theta_1(x, R, t) = \theta_2(x, R, t) \tag{36}$$

$$\frac{\partial\theta_1}{\partial r} - \varepsilon^2\frac{\partial R_1}{\partial x}\frac{\partial\theta_1}{\partial x} = \frac{h_1}{k_1}Bi(\theta_{\text{in}} - \theta_1)\left(1 + \varepsilon^2\left(\frac{\partial R_1}{\partial x}\right)^2\right)^{1/2} \quad \text{at } r = R_1 \tag{37}$$

$$\frac{\partial\theta_2}{\partial r} - \varepsilon^2\frac{\partial R_2}{\partial x}\frac{\partial\theta_2}{\partial x} = -\frac{h_2}{k_2}Bi(\theta_{\text{ex}} - \theta_2)\left(1 + \varepsilon^2\left(\frac{\partial R_1}{\partial x}\right)^2\right)^{1/2} \quad \text{at } r = R_2 \tag{38}$$

$$\frac{\partial\theta_1}{\partial r} - \varepsilon^2\frac{\partial R}{\partial x}\frac{\partial\theta_1}{\partial x} = \frac{k_2}{k_1}\left(\frac{\partial\theta_2}{\partial r} - \varepsilon^2\frac{\partial R}{\partial x}\frac{\partial\theta_2}{\partial x}\right) \quad \text{at } r = R \tag{39}$$

where $Ca_i = \mu_0 u_0/\sigma_i$ and $Ca = \mu_0 u_0/\sigma_{12}$ are capillary numbers, $Bi = h_0 R_0/k_0$ is the Biot number, h_0 is a constant reference value and h_i has been nondimensionalized with respect to h_0. Note that ρ, k and C_p have been assumed to be constant.

In order to clarify the relationships between dimensional and dimensionless quantities, Table 1 provides a summary of both the correspondence between the dimensional (denoted with asterisk) and dimensionless quantities and the nondimensional numbers used in this paper.

Assuming that $Re = \varepsilon\overline{R}$, $Fr = \varepsilon^{-1}\overline{F}$, $Ca_i = \varepsilon^{-1}\overline{C}_i$, $Ca = \varepsilon^{-1}\overline{C}$, $M^2 = \mathrm{O}(\varepsilon^4)$ and $Pr = \mathrm{O}(1)$, it is an easy matter to show that the above equations depend on ε^2. We, therefore, employ the following asymptotic expansions

$$\phi(x,r,t) = \phi_0(x,r,t) + \varepsilon^2\phi_2(x,r,t) + \mathrm{O}\big(\varepsilon^4\big) \tag{40}$$

for $\phi = u$, v, p and θ (and, therefore, μ), and

$$\psi(x,t) = \psi_0(x,t) + \varepsilon^2\psi_2(x,t) + \mathrm{O}\big(\varepsilon^4\big) \tag{41}$$

for R_1, R and R_2, in the governing equations and boundary conditions. The boundary conditions are then expanded in Taylor series with respect to ψ_0. To leading order, i.e., $\mathrm{O}(\varepsilon^0)$, the axial momentum equations and the shear conditions at the interfaces yield that $u_{i0} = B_i(x,t)$, whereas the continuity equation yields

$$v_{i0} = \frac{C_i}{r} - \frac{r}{2}\frac{\partial B}{\partial x} \tag{42}$$

where C_i is a function of x and t.

The radial momentum equations yield

$$p_{i0} = D_i - \mu_{i0}\frac{\partial B_i}{\partial x} - 2C_i \int \frac{1}{r^2}\frac{\mu_{i0}}{\partial r}\,\mathrm{d}r \tag{43}$$

whereas the kinematic conditions at the interfaces yield $C_1 = C_2$ and

$$\begin{aligned} C_1 &= \frac{\partial}{\partial t}\left(\frac{R_0^2}{2}\right) + \frac{\partial}{\partial x}\left(B\frac{R_0^2}{2}\right) = \frac{\partial}{\partial t}\left(\frac{R_{10}^2}{2}\right) + \frac{\partial}{\partial x}\left(B\frac{R_{10}^2}{2}\right) \\ &= \frac{\partial}{\partial t}\left(\frac{R_{20}^2}{2}\right) + \frac{\partial}{\partial x}\left(B\frac{R_{20}^2}{2}\right) \end{aligned} \tag{44}$$

where $\mu_{i0}(R_{j0}) \equiv \mu_{i0}(x, R_{j0}(x,t), t)$.

Use of the normal stress conditions at the interfaces yields

$$\begin{aligned} C_1 = \frac{1}{2}\Bigg[& p_{\mathrm{in}} - p_{\mathrm{ex}} - \frac{1}{\overline{C}_1 R_{10}} - \frac{1}{\overline{C} R_0} - \frac{1}{\overline{C}_2 R_{20}}\Bigg] \\ & \times \Bigg[\frac{\mu_{10}(R_{10})}{R_{10}^2} - \frac{\mu_{20}(R_{20})}{R_{20}^2} + \frac{\mu_{20}(R_0) - \mu_{10}(R_0)}{R_0^2} \\ & + \int_{R_{10}}^{R_0} \frac{1}{r^2}\frac{\partial \mu_{10}}{\partial r}\,\mathrm{d}r + \int_{R_0}^{R_{20}} \frac{1}{r^2}\frac{\partial \mu_{20}}{\partial r}\,\mathrm{d}r\Bigg]^{-1} \end{aligned} \tag{45}$$

and

$$D_1 = p_{\mathrm{in}} - 2\mu_{10}(R_{10})\frac{C_1}{R_{10}^2} - \frac{1}{C_1 R_{10}} \tag{46}$$

$$\begin{aligned} D_2 = {} & p_{\mathrm{ex}} - 2\mu_{20}(R_{20})\frac{C_2}{R_{10}^2} + \frac{1}{C_2 R_{20}} \\ & + 2C \int_{R_0}^{R_{20}} \frac{1}{r^2}\frac{\partial \mu_{20}}{\partial r}\,\mathrm{d}r \end{aligned} \tag{47}$$

Use of the axial momentum equation and shear stress conditions at $\mathrm{O}(\varepsilon^2)$ yields the following one-dimensional momentum equation

$$\begin{aligned} & (\rho_1 A_1 + \rho_2 A_2)\overline{R}\left(\frac{\partial B}{\partial t} + B\frac{\partial B}{\partial x}\right) \\ & = \frac{\overline{R}}{\overline{F}}(\rho_1 A_1 + \rho_2 A_2) \\ & \quad - A_1\frac{\partial D_1}{\partial x} - A_2\frac{\partial D_2}{\partial x} + \frac{\partial}{\partial x}\left(3(A_1\bar{\mu}_{10} + A_2\bar{\mu}_{20})\frac{\partial B}{\partial x}\right) \\ & \quad + \int_{R_{10}}^{R_0} \frac{\partial}{\partial x}\left(2C_1 \int_{R_{10}}^{r} \frac{1}{r^2}\frac{\partial \mu_{10}}{\partial r}\mathrm{d}r\right) r\,\mathrm{d}r \\ & \quad + \int_{R_0}^{R_{20}} \frac{\partial}{\partial x}\left(2C_1 \int_{R_0}^{r} \frac{1}{r^2}\frac{\partial \mu_{20}}{\partial r}\mathrm{d}r\right) r\,\mathrm{d}r \\ & \quad + 2C_1\left(\frac{\mu_{20}(R_{20})}{R_{20}}\frac{\partial R_{20}}{\partial x} - \frac{\mu_{10}(R_{10})}{R_{10}}\frac{\partial R_{10}}{\partial x}\right. \\ & \quad \left. + \frac{\mu_{10}(R_0) - \mu_{20}(R_0)}{R_0}\frac{\partial R_0}{\partial x}\right) \end{aligned} \tag{48}$$

where $A_1\bar{\mu}_{10} = \int_{R_{10}}^{R_0} \mu_{10} r\,\mathrm{d}r$, $A_2\bar{\mu}_{20} = \int_{R_0}^{R_{20}} \mu_{20} r\,\mathrm{d}r$,

$$A_1 = \frac{1}{2}\left(R_0^2 - R_{10}^2\right), \qquad A_2 = \frac{1}{2}\left(R_{20}^2 - R_0^2\right) \tag{49}$$

and Eq. (44) can be written as

$$\frac{\partial A_i}{\partial t} + \frac{\partial (A_i B)}{\partial x} = 0, \quad i = 1, 2 \tag{50}$$

$$\frac{\partial}{\partial t}\left(\frac{R_0^2}{2}\right) + \frac{\partial}{\partial x}\left(B\frac{R_0^2}{2}\right) = C_1 \tag{51}$$

Eqs. (48), (50) and (51) constitute a system of four equations for the four unknowns R_0, R_{10}, R_{20} and B, provided that μ_{10} and μ_{20} are known (cf. Eq. (19)).

So far, we have not employed the energy equation. This is due to the fact that the solution of this equation depends on the Biot number which, in turn, depends on the convective heat exchanges with the surrounding gases and the radiative heat exchanges between the hollow, compound fiber and the furnace walls in the neck-down region and between the fiber and the surroundings in the cooling region (Fig. 1). The Biot number is a function of temperature.

Here, we first assume that $Bi = h_0 R_0/k_0 = \varepsilon^2 \overline{B}$, where h_0 is a constant film heat transfer coefficient, and $h_i k_0/h_0 k_i$ are on the order of unity, for which the energy equation and the boundary conditions yield, to $\mathrm{O}(\varepsilon^0)$, $\theta_{10} = \theta_{20} = F(x,t)$, whereas, to $\mathrm{O}(\varepsilon^2)$, the energy equation and the thermal boundary conditions yield

$$\begin{aligned} & \overline{R}\,Pr\left(\frac{\partial}{\partial t}\left((\rho_1 C_{p1} A_1 + \rho_1 C_{p1} A_2)F\right)\right. \\ & \quad \left. + \frac{\partial}{\partial x}\left((\rho_1 C_{p1} A_1 + \rho_1 C_{p1} A_2)FB\right)\right) \\ & = \frac{\partial}{\partial x}\left((k_1 A_1 + k_2 A_2)\frac{\partial F}{\partial x}\right) + R_{10} h_1 \overline{B}(F - \theta_{\mathrm{in}}) \\ & \quad + R_{20} h_2 \overline{B}(F - \theta_{\mathrm{ex}}) \end{aligned} \tag{52}$$

where, again ρ_i, C_{pi}, h_i and k_i have been nondimensionalized with respect to ρ_0, C_{p0}, h_0 and k_0, respectively. The terms $h_1\overline{B}$ and $h_2\overline{B}$ in the above equations can be replaced by $\overline{B}_1 = h_1 R_0/k_0$ and $\overline{B}_2 = h_2 R_0/k_0$, respectively, where in these two expressions h_i, k_0 and R_0 are dimensional. In addition, $\overline{R}\,Pr$ can be replaced by a thermal Péclet number. The above equation is only valid for small Biot numbers and is a one-dimensional energy conservation equation.

For large Biot numbers, the one-dimensional equation (52) is not valid and one should use the time-dependent, two-dimensional energy equations for the two materials that compose the hollow, compound fiber subject to continuity of temperatures and heat fluxes at $R_0(x,t)$, $R_{10}(x,t)$ and $R_{10}(x,t)$, where the heat fluxes at $R_{10}(x,t)$ and $R_{20}(x,t)$ are analogous to those of the preform and, therefore, are not repeated here. In these two-dimensional equations, the slender fiber approximation can still be used to neglect $\mathrm{O}(\varepsilon^2)$-terms and the leading-order velocity components derived

in the asymptotic analysis for the convection terms, i.e., Eqs. (42) and (48), can be employed in the energy equation.

The above analysis shows that if $Bi = O(\varepsilon^2)$, the leading-order temperature along the hollow, compound fiber is only a function of x and t and, therefore, if the viscosity of the materials that constitute the fiber is only a function of the temperature, then the integral terms in the leading-order momentum equation (cf. Eq. (45)) are nil. However, if Bi is on the order of $O(\varepsilon^0)$, heat losses/gains enter the energy equation at leading order, i.e., the temperature field is two-dimensional and the integral terms in the leading-order momentum equation are not nil.

The one-dimensional equations (48), (50)–(52) are subject to initial at $t = 0$ and boundary conditions at $x = 0$ and $x = 1$, i.e., at the axial locations where the preform melts and the hollow, compound fiber is collected, respectively. In general, the values of R_{10}, R_0 and R_{20}, B and F are specified at $x = 0$ and correspond to those of the preform at its melting temperature. In the case of glass fibers drawn from a melt, i.e., $L_p = 0$, averaged values of the velocity and temperature must be used to determine both B and F at $x = 0$. In addition, downstream boundary conditions are to be specified for both B and F at $x = 1$. In the calculations reported here, $B(1, t)$ was specified and a no heat flux condition was used at $x = 1$. Note that the one-dimensional energy equation is of second-order in x.

2.3. Governing equations for the gases surrounding the fiber

The motion of the gases surrounding the preform and fiber was assumed to be axisymmetric. These gases were considered to be either incompressible or compressible; in both cases, the gas dynamic viscosity, specific heat at constant pressure and thermal conductivity were assumed to be constant and the viscous dissipation rate was neglected. In the first case, the Boussinesq approximation was employed and the governing equations can be written as

$$\frac{\partial u}{\partial x} + \frac{1}{r}\frac{\partial}{\partial r}(rv) = 0 \tag{53}$$

$$\rho_0 \frac{Du}{Dt} = -\frac{\partial p}{\partial x} + \mu\frac{\partial^2 u}{\partial x^2} + \frac{\mu}{r}\frac{\partial}{\partial r}\left(r\frac{\partial u}{\partial r}\right) + \rho_0 g\beta(T - T_0) \tag{54}$$

$$\rho_0 \frac{Dv}{Dt} = -\frac{\partial p}{\partial r} + \mu\frac{\partial^2 v}{\partial x^2} + \frac{\mu}{r}\frac{\partial}{\partial r}\left(r\frac{\partial v}{\partial r}\right) - \frac{\mu v}{r^2} \tag{55}$$

$$\rho_0 C_p \frac{DT}{Dt} = k\frac{\partial^2 T}{\partial x^2} + \frac{k}{r}\frac{\partial}{\partial r}\left(r\frac{\partial T}{\partial r}\right) \tag{56}$$

where ρ_0 and T_0 are a reference density and a reference temperature, respectively, and β is the thermal expansion coefficient which is assumed to be constant.

For compressible gases, Eqs. (53)–(56) are valid with the following exceptions: ρ_0 is not constant, Eq. (53) must be replaced by its compressible counterpart, i.e., $\frac{\partial \rho_0}{\partial t} + \frac{\partial}{\partial x}(\rho_0 u) + \frac{1}{r}\frac{\partial}{\partial r}(r\rho_0 v) = 0$, the gases are assumed to be ideal $p = \rho_0 \mathbf{R} T$, where $\mathbf{R}$ is the gas constant, and the last term of Eq. (54) must be replaced by $\rho_0 g$.

2.4. Radiative heat transfer model

The net radiative method for enclosures [17] was used to determine the thermal radiative heat flux, i.e., q_r, to each surface, including the preform and fiber and the furnace walls and irises. To that end, the preform, fiber and vertical wall of the furnace were divided into exterior ring elements, and the bottom and top walls of the furnace, i.e., the irises, were divided into annular elements. For each element,

$$\sum_{j=1}^{j=N}\left(\frac{\delta_{kj}}{\varepsilon'_j} - F_{k-j}\frac{1-\varepsilon'_j}{\varepsilon'_j}\right)q_{rj} = \sum_{j=1}^{j=N} F_{k-j}\sigma\left(T_k^4 - T_j^4\right) \tag{57}$$

where N is the number of elements, δ_{kj} is the Kronecker's delta ($\delta_{kj} = 1$ if $k = j$, and 0, otherwise), σ is the Stefan–Boltzmann constant, and F_{k-j} are the view factors which were determined by direct numerical integration.

Since the sum of each element's view factors must be equal to unity, we imposed this constraint in the above equation, because calculations performed without this constraint showed that the sum of each element's view factors was within 0.5% of unity. In addition, for slender fibers, the outer surface of the fiber was approximated by the surface of a cone for the calculation of the view factors. This approximation is not expected to introduce large errors, while it avoids the need for the calculation of the view factors at each iteration of the numerical technique used to solve the equations for the preform, the fiber and the gases surrounding the fiber.

The simultaneous solution of Eq. (57) for all the surfaces provides the net radiative heat transfer flux at the preform and fiber's outer surfaces. At these surfaces, the temperature is continuous and there is no jump in the heat fluxes, e.g., $-k_2\frac{\partial T_2}{\partial n}(x, R_2, t) \equiv q_2 = -k_g\frac{\partial T_g}{\partial n}(x, R_2, t) + q_r(R_2)$, where $q_r(R_2)$ denotes the net radiative heat transfer flux determined from Eq. (57). In addition, q_2 may be used in the fiber's one-dimensional energy equation to determine the local film heat transfer coefficient, since $q_2 = h_2(T_2(x, R_2, t) - T_{ex})$.

The top and bottom (irises) walls of the furnace were assumed to be isothermal with constant temperatures equal to T_T and T_B, respectively; the vertical wall of the furnace was also assumed to be isothermal but with a temperature that was parabolic and exhibited a relative maximum at mid-height. The boundary conditions at the preform and fiber outer surfaces were incorporated into the energy equation for the gas as indicated above.

No-slip boundary conditions were applied at the furnace top, bottom and vertical walls and at the fiber's outer interface and at the outer surface of the preform. Notice that these boundary conditions are a simplification of the real ones because the outer surface is a material surface where the tangential stresses are continuous and the jump in normal stresses must be balanced by surface tension. However,

since the dynamic viscosity of gases is much smaller than that of the fiber material, the gases may be considered as passive for the fiber, and the fiber may be considered as a rigid material for the gases. The errors incurred by not imposing boundary conditions on the tangential and normal stresses at the fiber's outer surface when solving the equations for the gases that surround the hollow, compound jet are expected to be small and, therefore, the approximation presented here may be a good one, even though its accuracy was not assessed by comparing the numerical results presented here with those of other calculations which incorporate the kinematic and dynamic coupling between the fiber and the gases that surround it.

3. Numerical methods

The conduction heat transfer equations for the preform were discretized by using a control-volume formulation, second-order accurate finite differences in the axial and radial directions, and first-order accurate, backwards difference in time, i.e., an implicit method. The resulting set of linear algebraic equations was solved by means of LU-decomposition upon using the interface boundary conditions at $R_0(x,t)$. Since q_1 and q_2 have to be determined as part of the solution, they were treated as source terms and iterations were preformed until convergence was achieved. This iterative Picard procedure has the advantage that the LU-decomposition is determined only once, although the method exhibits only a linear rate of convergence.

The one-dimensional equations for the hollow, compound fiber geometry, axial velocity, and temperature when the Biot number is $O(\varepsilon^2)$, were also discretized by means of a control-volume formulation and first-order backward differences in time, second-order accurate finite differences for the diffusion terms, and upwind differences for the convection ones, and the resulting system of nonlinearly coupled equations was solved iteratively until convergence was achieved.

For Biot numbers of order of unity, the hollow, compound fiber is governed by one-dimensional equations for its geometry and axial velocity component, whereas the fiber's temperature is governed by two-dimensional equations which use the leading-order axial and radial velocity components determined in the asymptotic analysis described previously. In this case, we also employed a control-volume formulation, backward differences in time, upwind discretizations for the convection terms, and central differences for the diffusion processes, and the system of nonlinearly-coupled equations was solved iteratively until convergence was achieved.

In both the incompressible and the compressible gas cases considered in this study, the governing equations for the gases were discretized in control volumes using a staggered grid where the scalar variables were determined at the centers of the control volumes, while the velocity components were determined at the faces of these volumes. A power-law technique was used to discretize the convective fluxes, and a pressure-correction algorithm based on that of the SIMPLE technique [18] was employed in the calculations. The ordinary differential equations resulting from the integration of the gas equations in control volumes were discretized by means of an implicit, first-order accurate, backward Euler method. Due to the coupling of the gas equations, under-relaxation factors equal to 0.5 and 0.8 were used to solve the discretized forms of the momentum and energy equations, respectively. An under-relaxation factor equal to 0.1 was used in the pressure correction algorithm.

The calculations were preformed as follows. First, the equations of the net radiative model for enclosures were solved with guessed temperatures at the preform and at the fiber's outer surfaces. This model provides the radiative heat fluxes on the surfaces of the fiber, furnace and preform. We then solved the equations for the gases surrounding the preform and fiber and determined the total (convective + radiative) heat fluxes on their surfaces. Finally, the equations for the preform and fiber were solved, and the whole iterative cycle was repeated until convergence was achieved. Note that, in addition to the global (outer) iterative procedure, inner iterations were preformed to determine the fluid and/or thermal fields in the preform, the fiber and the gases surrounding the fiber until their respective governing equations converged. This inner-and-outer iterative procedure was found to converge rapidly for the case of optical fibers where the temperature differences are not very large, but was found to be rather slow when the temperature differences are large. In this case, it may prove to be more efficient to solve all the equations simultaneously and employ a Newton method rather than the Picard algorithm employed in this study. It must be noted that, in all the calculations presented in this paper, no gases were assumed to be enclosed by the fiber's inner surface, i.e., $q_1 = 0$.

The time step employed in the calculations was varied from 0.1 to 0.001 in order to ensure time-step independent results, whereas the number of grid points employed in the radial and axial directions was also varied to obtain almost grid-independent results.

In the calculations reported here, the grid spacing in the gases surrounding the fiber was constant in the x and r directions, and the number of grid points in these directions was 500 and 50, respectively. Calculations were also preformed with unequally-spaced grids in the r direction which concentrate the grid points near the preform and at fiber's outer surface, but it was found that a 500×50-point equally-spaced grid provides results within 1% of those obtained with the unequally-spaced grid. Convergence within the time step was assumed to occur when the residuals of the momentum and energy equations were equal to or less than 10^{-6}. It must be pointed out that the time-dependent equations were also used to determine the steady state solution because the discretization of the time derivatives increases the diagonal dominance of the discretized equations.

4. Results

The models presented in previous section have been used in the heating region and in the cooling region (cf. Fig. 1). In the heating region, the coupled model was used to determine the temperature distribution in both the preform and the fiber (cf. Fig. 3) by means of the coupled model discussed before, while, in the cooling region, only the one-dimensional model was employed. It must be emphasized that the coupled model considers the two-dimensional temperature distribution in the preform, whereas the fluid dynamics and heat transfer of the fiber are analyzed by means of the one-dimensional model. Moreover, since the formulation presented in this paper can be applied to both silica and polymer optical fibers, we have performed simulations with the coupled model for silica optical fibers.

4.1. Results of the coupled model

We shall first describe the results obtained with the coupled model that includes radiative heat exchanges in the furnace, convection in the gases that surround the preform and fiber, and the one-dimensional equations for the hollow, compound fiber's geometry, axial velocity component and temperature. This coupled model requires very long computational times to achieve convergence for the conditions described below and the grid size and time step discussed above. For example, a simulation using the Boussinesq approximation required 36 hours 25 minutes of CPU time in a two-processor 600 MHz HP J5600 workstation, whereas a similar simulation with the compressible flow equations for the gases surrounding the preform and hollow, compound fiber required 62 hours 11 minutes of CPU time in the same workstation. Due to the long computational times required by the coupled model, only four simulations were performed with this model. Two of these simulations were carried out with the incompressible flow approximation for the gases surrounding the fiber with and without the Boussinesq approximation in order to determine the importance of natural or free convection. The other two simulations were carried out by assuming that the gases that surround the hollow, compound fiber are compressible, and either considering or neglecting the gravitational term in the axial momentum equation.

Unless otherwise stated, the calculations reported in this section correspond to pure silica, $L_f = 30$ cm, $R_1(0,t) = 0.5$ cm, $R(0,t) = 0.75$ cm, $R_2(1,t) = 1$ cm, $L_p = 10$ cm, take-up speed of 300 cm·s^{-1}, a melting temperature of 1900 K and $T_{\mathrm{ex}} = 1373$ K, and a draw ratio, i.e, the ratio of the axial velocity at the take-up point to that at the preform's tip, i.e., at $x = L_p$, equal to 100. In addition, the reference temperature used in the calculations is that corresponding to the melting point, and the properties of the gases in the furnace were assumed to be constant and equal to those of air. Note that the temperature at which the preform was fed into the furnace was determined numerically by trial and error in order to assure that the melting temperature was reached at L_p. In real optical fiber drawing processes, one should account for the heating/cooling part of the preform outside the furnace which is also governed by the heat conduction equations employed to determine the temperature of the preform within the furnace in the formulation presented in this paper.

For the conditions described above, emissivities of the fiber, irises and furnace vertical walls equal to 0.90, 0.75 an 0.75, respectively, temperatures of the top and bottom irises equal to 2000 °C, and a parabolic temperature of the furnace's vertical wall which exhibited a relative maximum equal to 2500 °C at midheight and had a value of 2000 °C at the corners between the furnace cylindrical wall and the irises, it has been found that forced convection is much more important than free convection, and errors of less than 1% were incurred by neglecting the gravitational term in the momentum equations for the gases surrounding the hollow, compound fiber. This is not surprising in glass optical fibers where the furnace temperature and the take-up velocity are high. This comment may not apply to polymeric optical fibers that are drawn at lower temperatures and axial velocities, and, therefore, free convection may be as important as or more important than forced convection. The same comment also applies to the drawing of conventional glass or textile fibers where cooling gases are forced in a direction perpendicular to the fiber's axis.

The motion of the gases surrounding the fiber exhibited complex features, i.e., recirculation zones, characterized by downward motion along the fiber, upward motion along the furnace vertical wall, and horizontal motions along the irises or top and bottom walls of the furnace. The gas motion along the top iris was inwards whereas that along the bottom one was outwards, and regions of high vorticity were observed at the corners of the furnace.

For the conditions described above, the recirculating flow patterns in the gases surrounding the fiber were found to be nearly steady ones when the Boussinesq approximation was used in the axial momentum equation. Calculations performed with the compressible equations were not found to differ much from those obtained with the Boussinesq approximation, except near the corners and hot irises and furnace wall, although the compressible flow model was found to require much longer computational times as stated above.

For the conditions considered in this paper, it was observed that radiative heat exchanges accounted for about 71% of the total heat exchanges, whereas convective ones accounted for about 29%. These values represent averaged quantities along the fiber, and indicate that radiative heat exchanges are more important than convective ones; however, the latter cannot be neglected. Most importantly, however, is the fact that the fiber geometry obtained with the coupled model under these conditions was quite similar to that observed with only the one-dimensional model for the hollow, compound fiber using a constant Biot number equal to 85. In fact, it has been observed that for the same conditions as those considered in the next subsection, the coupled

model provided analogous results to those of only the one-dimensional model for hollow, compound fibers when the latter employed an adequately chosen constant Biot number.

Fig. 5 (top) shows the temperature at the outer surface of the preform and fiber as a function of the axial distance along the furnace. This figure indicates that the fiber's surface temperature increases from approximately a value of 0.8 at $x = 0$ to about 1.06 at about $x = 0.42$ and then decreases until reaching a zero gradient at the furnace exit, i.e., $x = 1$. Fig. 5 (top) also indicates that, if the one-dimensional model for the fiber is used with a Biot number equal to 85, the temperature predicted by this one-dimensional model is slightly higher than if the same model accounts for the detailed convective an radiative heat exchanges between the fiber and the furnace walls.

Fig. 5 (bottom) shows that the difference between the temperature at the compound fiber's surface and that at the inner one first increases and then decreases and tends to a nil value along the furnace, and that this difference is small. This figure also illustrates the fast increase in the preform temperature as it enters into the furnace.

Fig. 6 illustrates the preform and fiber geometries in the furnace. As indicated before, the preform was assumed to be rigid and preserves its diameter up to $x = L_p = 0.3$. The hollow, compound fiber's radii decrease in an almost exponential manner for $L_p \leqslant x \leqslant L_f$.

The results presented in Figs. 5 and 6 exhibit similar trends to those of Figs. 5–7 of Lee and Jaluria [11] despite the differences in the preform and fiber geometry and the fact that these authors did not consider the motion of the gases that surround the preform and fiber, although they accounted for the fluid dynamics of the melt in both the preform and the fiber by means of a stream function-vorticity formulation. Lee and Jaluria [11] also considered a solid core optical fiber. However, these authors predicted higher surface temperatures than the ones reported in Fig. 5 of this paper. In addition, the fiber temperature at the furnace exit was almost equal to the melting temperature, whereas the results presented in Fig. 5 indicate that, in our calculations, the fiber temperature at the furnace exit is lower than the melting temperature.

Although the coupled model presented here can be used to study time-dependent phenomena, only steady calculations have been reported, even though the unsteady formulation was used to determine the steady state solution, because it was found that, due to the nonlinear coupling between radiation and convection, the discretization of the time-transient terms helped to accelerate the convergence of the iterative technique employed in these studies.

During the review process of this paper, further simulations with the coupled problem were performed in order to determine the effects of the emissivities of the fiber, preform, irises and furnace wall on the fiber's geometry. These simu-

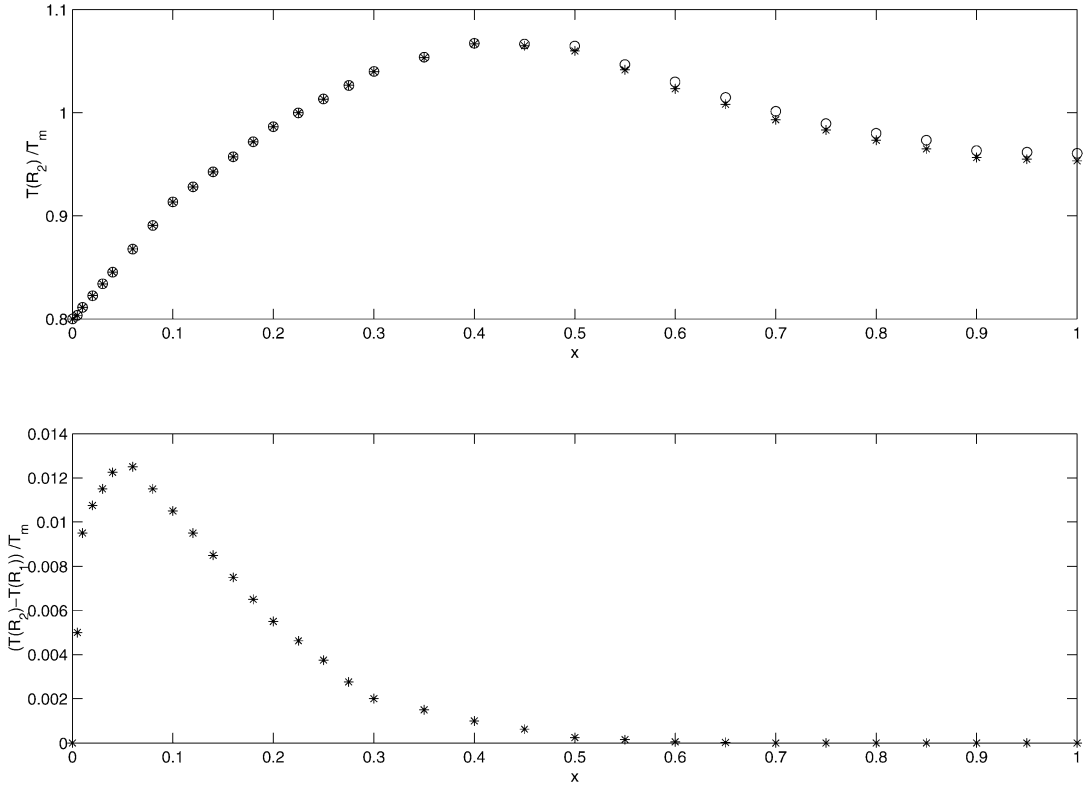

Fig. 5. Nondimensional temperature of the fiber's outer surface, $T(R_2)/T_m$, (top) and difference between the temperature of the outer and inner surfaces of the hollow, compound fiber, $(T(R_2) - T(R_1))/T_m$, (bottom) as functions of the nondimensional axial distance along the furnace. (Coupled model with detailed analysis of radiative and convective exchanges: $*$; coupled model with a constant Biot approximation for the one-dimensional model of the fiber: $\circ$.)

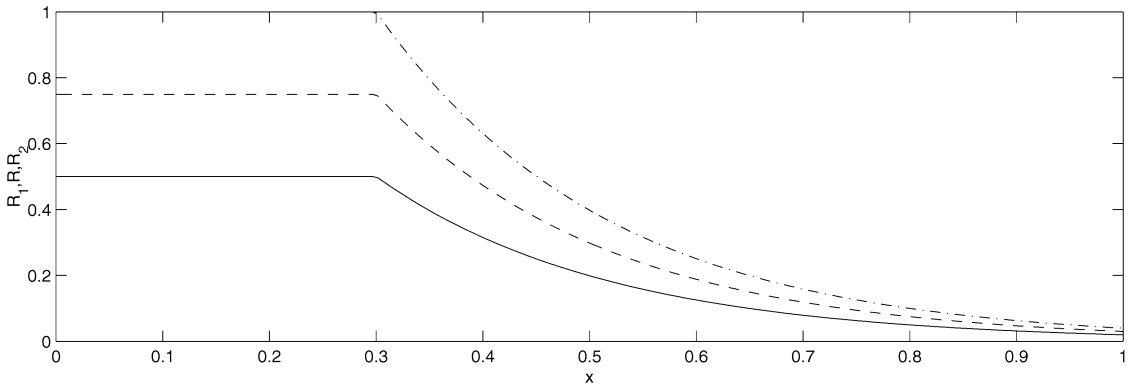

Fig. 6. Nondimensional geometry of the fiber as a function of the nondimensional axial distance along the furnace. (Solid line: inner surface; dashed line; interface between the inner and outer materials; dashed–dotted line: outer surface.)

lations indicate that the emissivities play a paramount role in determining the heat exchange processes and the fiber fluid dynamics. An important role in the heating process taking place in the furnace is also played by the temperature of the irises and furnace wall, and the necking location was found to be strongly affected by the thermal boundary conditions. This has important consequences on the stability and control of the manufacturing of optical fibers. More importantly, however, is the fact that, in all of these cases, the coupled model provided analogous results to those of only the one-dimensional model for hollow, compound fibers when the latter employed an adequately chosen constant Biot number (cf. Fig. 5 (top)).

4.2. Results of the one-dimensional fiber model

We shall next report some steady state results obtained with only the one-dimensional model for hollow, compound fibers without taking into consideration the motion of the gases surrounding the fiber, and using constant Biot numbers, i.e., h_1 and h_2 are assumed constant. As stated above, this one-dimensional is valid in the cooling region. Note that, if the preform's length is much larger than its characteristic radius, the preform is slender and its temperature equation is analogous to that derived for the hollow, compound fiber.

The first results shown in this section are relevant to both melt spinning for $x_1 \leqslant x \leqslant x_2$ and optical fiber drawing processes for $L_p \leqslant x \leqslant L_f$, correspond to a nondimensional temperature and axial velocity component of the fiber at the die equal to one, a take-up speed equal to 100, $\overline{R} = \overline{F} = \overline{C} = \sigma/\sigma_2 = \sigma_1/\sigma_2 = S_1/S_2 = k_2/k_1 = 1$, $h_1 = p_{\text{in}} - p_{\text{ex}} = \theta_{\text{ex}} = 0$, $R(0) = 1$, $R_1(0)$ and $R_2(0)$ can be determined from the conditions that the (nondimensional) volumetric flow rate for the inner and outer annular jets is 0.5, and consider the effects of the activation energies E_1 and E_2, Péclet number and Biot number Bi_2 on the hollow, compound fiber drawing process, since the effects of the pressure difference, Reynolds, Froude and capillary numbers, surface tension ratios, fiber's radii at the die and volumetric flow rates were found to exhibit similar trends to those observed under isothermal conditions [6]. Since these results are of relevance to both conventional and optical fiber drawing processes, it must be emphasized that there is no preform in the former and that the coordinate x that appears below refers to the axial location measured from the die's exit and the melting point of the preform for conventional and optical fiber drawing processes, respectively. In addition, we shall use the term "die exit" to refer to the true die exit in the case of conventional fiber drawing processes or the location where the preform melts in the case of optical fiber drawing.

Table 2
Values of parameters

Figure	E_1	E_2	Pe_1	Pe_2	$\overline{B}$	k_2/k_1	S_2/S_1
7	100	100	100	100	var.	1	1
8	var.	100	100	100	10	1	1
9	100	var.	100	100	10	1	1
10	100	100	100	var.	10	1	1
11	100	100	100	100	10	var.	1
12	100	100	100	100	10	1	var.

Fig. 7 illustrates the effects of Bi_2 for the conditions of Table 2 and indicates that the temperature drop increases as the Biot number is increased. This temperature drop results in a large increase in the dynamic viscosity of the materials that compose the fiber, and a necking phenomenon near the die's exit whose magnitude increases as the Biot number is increased. Fig. 7 also shows that, at large Biot numbers, the increase in dynamic viscosity results in an almost constant axial velocity beyond the necking region, and that the temperature drop for the largest Biot number considered in the figure is about 18%. The reader is cautioned that the results presented in Fig. 7 as well as in the other figures presented in this paper are nondimensional, i.e., the radii and axial length have been nondimensionalized with respect to R_0 and $L \equiv L_f - L_p$, respectively, and that $R_0/L = \varepsilon \ll 1$, and, therefore, the necking in dimensional coordinates does not occur as close to the die as the results presented in Fig. 7 seem to indicate.

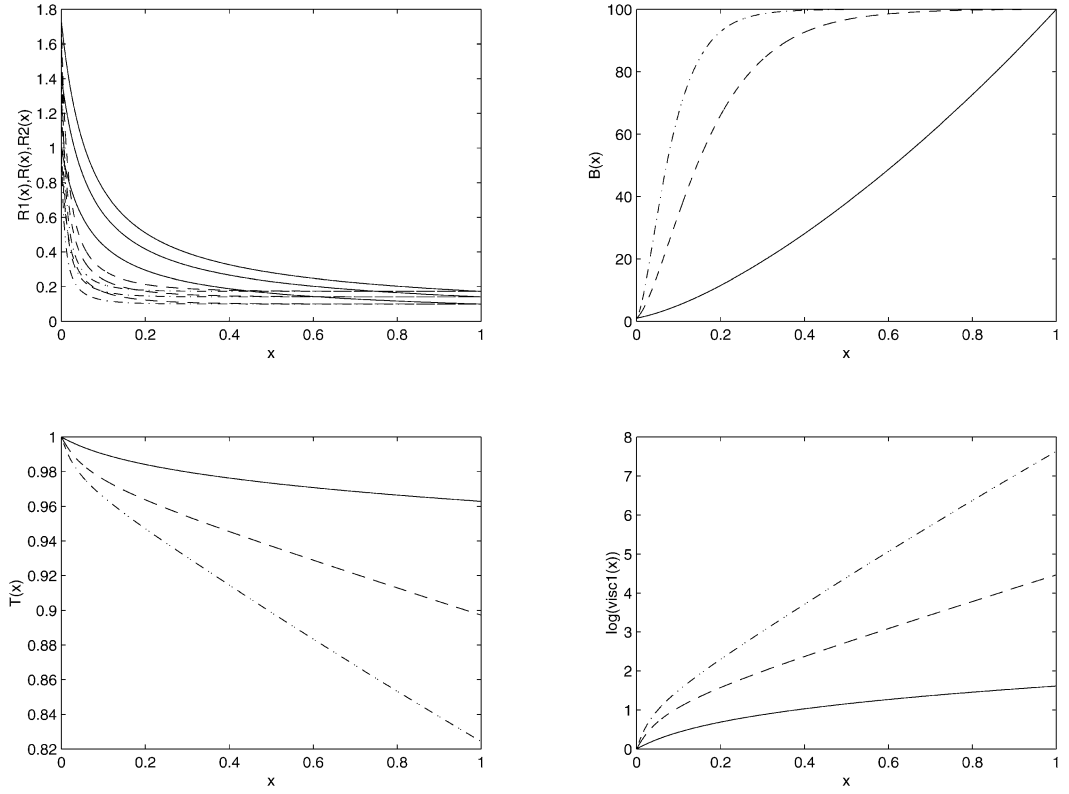

Fig. 7. Steady state fiber's geometry (top left), axial velocity component (top right), temperature (bottom left) and viscosity of the inner material (bottom right). Solid line: $\overline{B} = 10$; dashed line: 50; dashed–dotted line: 100.

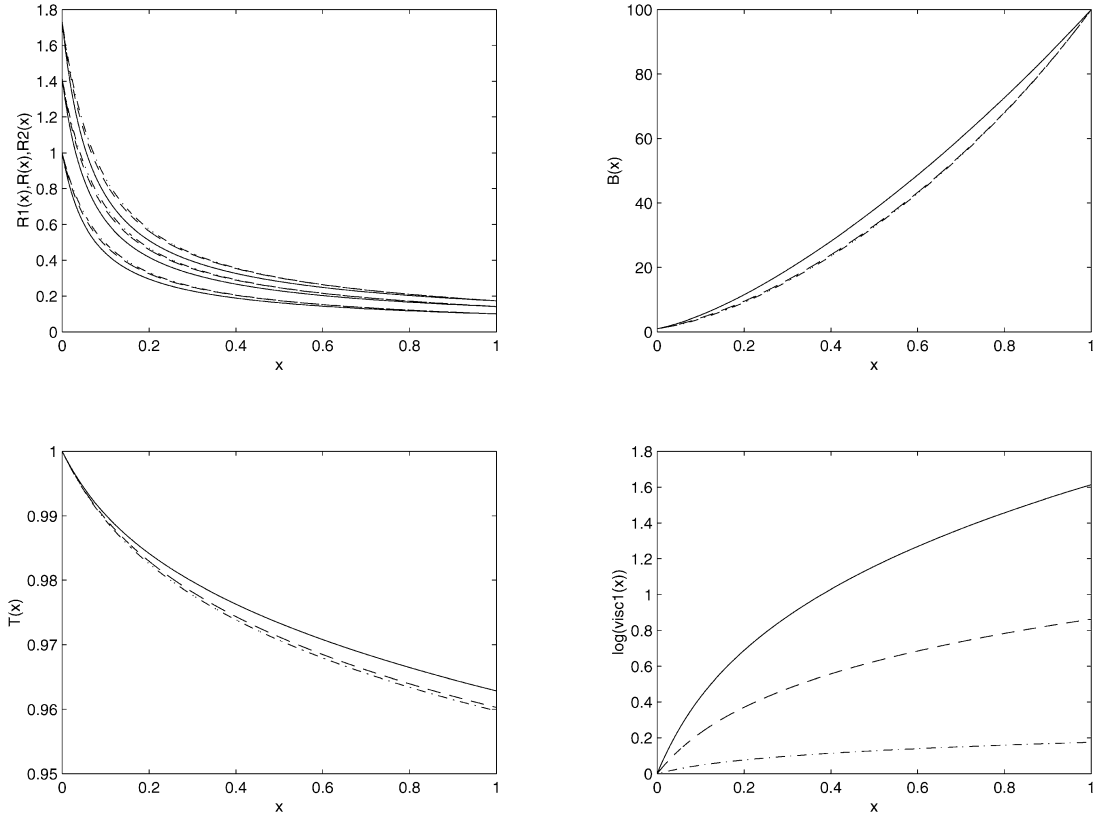

Fig. 8. Steady state fiber's geometry (top left), axial velocity component (top right), temperature (bottom left) and viscosity of the inner material (bottom right). Solid line: $E_1 = 100$; dashed line: 50; dashed–dotted line: 10.

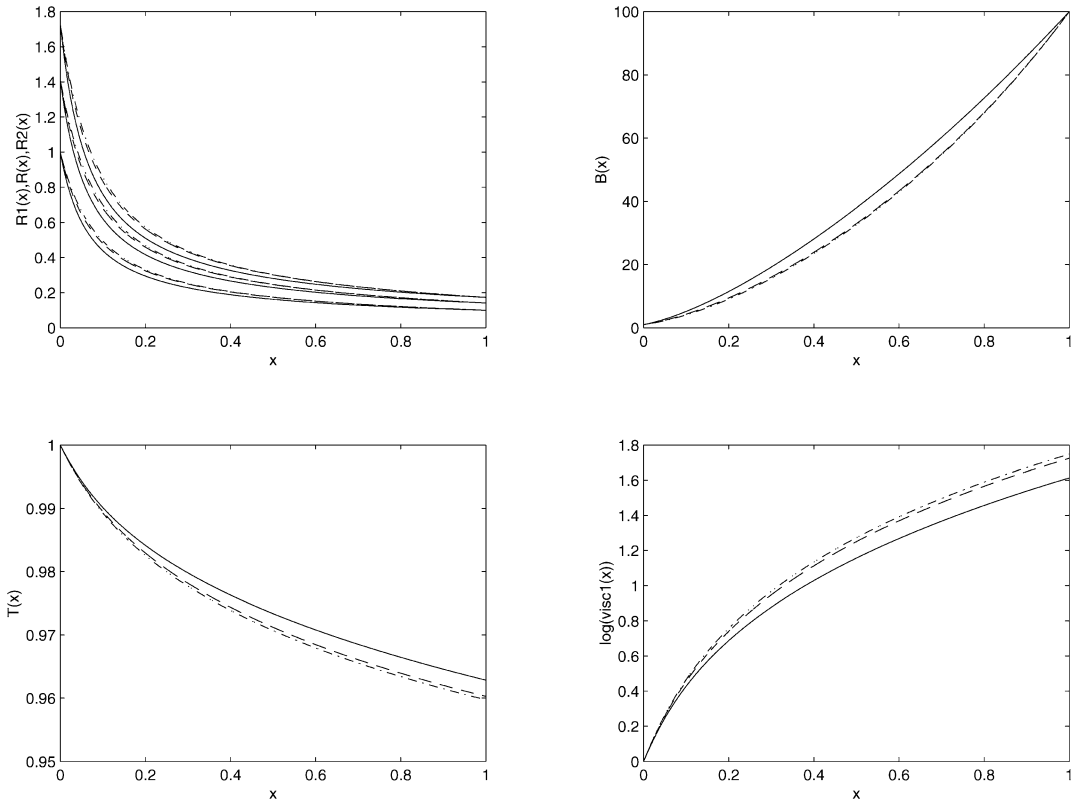

Fig. 9. Steady state fiber's geometry (top left), axial velocity component (top right), temperature (bottom left) and viscosity of the inner material (bottom right). Solid line: $E_2 = 100$; dashed line: 50; dashed–dotted line: 10.

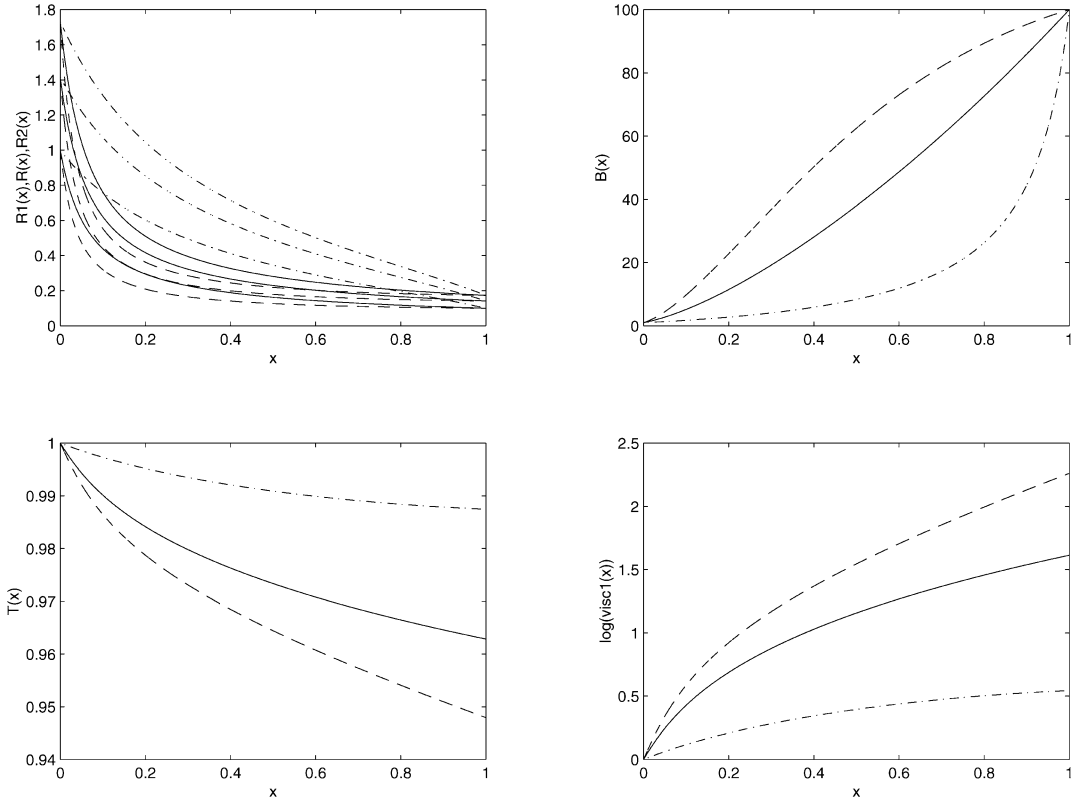

Fig. 10. Steady state fiber's geometry (top left), axial velocity component (top right), temperature (bottom left) and viscosity of the inner material (bottom right). Solid line: $Pe_2 = 100$; dashed line: 10; dashed–dotted line: 1000.

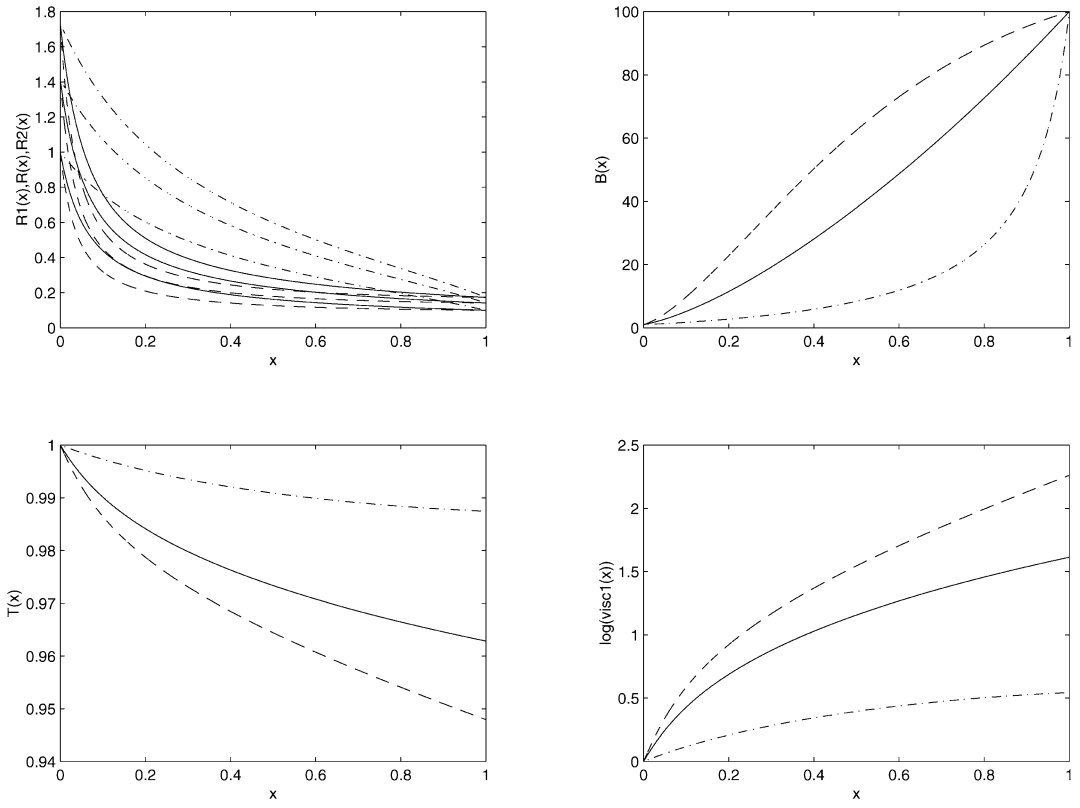

Fig. 11. Steady state fiber's geometry (top left), axial velocity component (top right), temperature (bottom left) and viscosity of the inner material (bottom right). Solid line: $k_2/k_1 = 1$; dashed line: 0.01; dashed–dotted line: 100.

The effects of the (nondimensional) activation energy E_1 on the fiber geometry, velocity and temperature are shown in Fig. 8 and indicate that, for the parameters considered in this figure, the effects of E_1 are small. In addition, the axial velocity, temperature and the dynamic viscosity at a given axial location increase as E_1 is increased. The apparent paradox for the temperature and viscosity shown in Fig. 8 is a consequence of the values of the parameters used in the calculations and the fact that the fiber's geometry and the momentum equation are controlled by the viscosities of both the inner and outer materials. In Fig. 8, the main contribution to the momentum diffusion is associated with the outer material whose viscosity increases much more rapidly than that of the inner when $E_2 > E_1$. This point is emphasized in Fig. 9 which shows that the effects of E_2 on the fiber geometry, axial velocity component and temperature are analogous to those of E_1; however, the effects of E_2 on the dynamic viscosity of the inner material are opposite to those of E_1.

The effects of Pe_2 are exhibited in Fig. 10 that shows that the axial velocity profile, temperature, geometry and dynamic viscosity of the inner material are strong functions of the Péclet number for the outer material. Fig. 10 also shows the changes in the concavity of the axial velocity profile as functions of Pe_2. Note that, as the magnitude of the Péclet number is increased, the magnitude of the convection terms in the energy equation increases and the cooling of the fiber decreases. Similar results to those of Fig. 10 have also been observed when Pe_1 was varied.

The results presented in Fig. 10 indicate that, at large thermal Péclet numbers, the fiber's geometry is like that observed under isothermal conditions [6] and exhibits an axial gradient different from zero at the take-up point, i.e., at $x = 1$. On the other hand, heat transfer effects are important for Péclet numbers less than or equal to 100 and the fiber exhibits a necking phenomenon the magnitude of which increases as the Péclet number is decreased. Although not shown here, similar results to those presented in Fig. 10 have also been observed when Pe_1 was varied.

Fig. 11 exhibits the effects of k_2/k_1 on the hollow, compound fiber and indicates that, as this ratio is increased, the necking region moves toward the die's exit, the axial velocity component and dynamic viscosity increase and the temperature decreases. For small thermal conductivity ratios, the fiber temperature decreases slowly along the fiber and the axial velocity has similar trends to those observed in isothermal melt spinning processes. Note that the axial velocity is almost linear for $k_2/k_1 = 1$.

The effects of S_2/S_1 on the fiber dynamics are small as shown in Fig. 12 which indicates that the axial velocity and temperature increase as this ratio is increased. One might have expected the opposite trend; however, the radius R of the interface between the two materials of the fiber depends

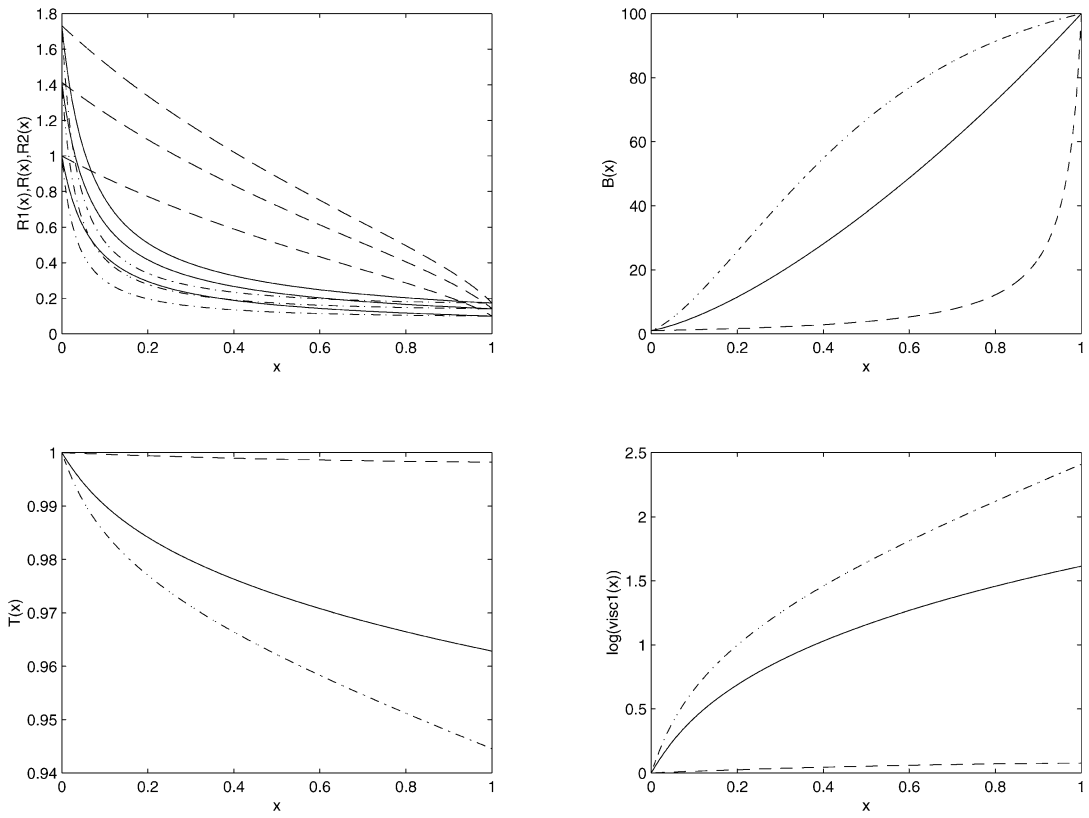

Fig. 12. Steady state fiber's geometry (top left), axial velocity component (top right), temperature (bottom left) and viscosity of the inner material (bottom right). Solid line: $S_2/S_1 = 1$; dashed line: 0.01; dashed–dotted line: 100.

in a complex manner on the viscosity ratio as indicated in Eqs. (45) and (48).

Transient calculations were also performed with the one-dimensional model in order to analyze the dynamic response of the hollow, compound fiber to sinusoidal time-dependent volumetric flow rates and temperature at the die and at the take-up point. The results of these calculations which use constant or space-dependent Biot numbers, show that non-isothermal fibers are more stable than isothermal ones, and the critical take-up velocity ratio at which the draw resonance of isothermal fibers is observed can be substantially exceeded without the fiber losing its stability. This is not to say that draw resonance does not occur in nonisothermal fibers, rather, if it does occur it takes place at higher take-up speeds than under isothermal conditions.

5. Conclusions

A coupled model for the study of hollow, compound optical fiber drawing processes has been developed. The model accounts for the heat transfer in the preform and fiber and for the motion of the gases surrounding the preform and fiber by means of two-dimensional equations, employs a net radiative heat exchange model for the radiative heat exchanges amongst the preform, fiber, irises and furnace walls, and uses asymptotically-derived one-dimensional equations for the geometry, axial velocity component and temperature along the fiber for small Biot numbers. At high Biot numbers, the geometry and axial velocity component of the fiber are governed by one-dimensional equations that depend on the cross-sectional averages of the dynamic viscosity, while the temperature field in the fiber is governed by a two-dimensional energy equation.

The model neglects latent heat effects associated with the melting of the preform and the fiber melting/solidification, and uses a Newtonian rheology, but employs a dynamic viscosity law that increases exponentially as the temperature drops below its melting point. It also includes either a Boussinesq approximation in the momentum equations or a compressible formulation for the gases that surround the fiber. In either case, the models for the preform, fiber and gases surrounding the fiber are solved separately and iteratively until convergence is achieved, and the radiative heat transfer model assumes that the fiber has a conical shape, and nonparticipating gases.

Simulations with the coupled model that accounts for radiative heat exchanges and the motion of the gases surrounding the preform and fiber show that, for the conditions presented in this paper, radiative heat exchanges are about three times larger than forced convection effects, free convection is not important, and the fiber's geometry, axial velocity and temperature predicted by the coupled model are in remarkable good agreement with those obtained with the

one-dimensional model for hollow, compound fibers and a suitable constant Biot number.

Calculations performed with the one-dimensional hollow, compound fiber model by itself using a constant Biot number along the fiber indicate that, as the Biot number is increased, the heat losses and the fiber's dynamic viscosity increase, the fiber exhibits a strong necking phenomenon and the fiber's axial velocity increases rapidly from its value at the die's exit to a constant value downstream and then remains constant.

For the conditions considered in this paper, it has been observed that the activation energies of the viscosity laws for the inner and outer materials of the hollow, compound fiber do not have very strong effects on the fiber's geometry, axial velocity component and temperature, whereas the fiber's solidification point moves towards the die as the thermal Péclet number is decreased. The effects of the pre-exponential factor of the viscosity law were found to not strongly affect the fiber's geometry, motion and thermal field.

The fact that only the one-dimensional model for hollow, compound fibers with a properly selected constant Biot number may predict results in accord with those of the more complex and expensive coupled model that accounts for radiative heat exchanges and the motion of the gases that surround the fiber, indicates that, at least for the conditions considered here, substantial savings can result from developing accurate correlations for an effective film transfer coefficient that includes the effects of convection and radiation, although the design of the heating furnace and irises may require the use of the coupled model.

Acknowledgements

This research was partially financed by project BFM2001-1902 from the Ministerio de Ciencia y Tecnología of Spain and fondos FEDER. This paper is a substantially extended and revised version of the one presented at *CHT-04: An ICHMT International Symposium on Advances in Computational Heat Transfer*, held on board of MS Midnatsol on the coast of Norway on 19–24 April 2004, organized by G. de Vahl Davis and E. Leonardi of the University of New South Wales, Australia, and published by Begell House, New York, in 2004 as CD-ROM Proceedings, ISBN 1-5670-174-2. The author kindly appreciates the recommendation of Professor Graham de Vahl Davis to submit this paper to this journal. The author is also grateful to the referee for his comments that have resulted in both an improvement of the presentation and the elimination of some errors.

References

[1] T.M. Monro, D.J. Richardson, N.G.R. Broderick, P.J. Bennett, Holey optical fibers: An efficient modal model, J. Lightwave Technol. 17 (1999) 1093–1102.
[2] C.M. Smith, N. Venkataraman, M.T. Gallagher, D. Müller, J.A. West, N.F. Borrelli, D.C. Allan, K.W. Koch, Low-loss hollow-core silica/air photonic bandgap fibre, Nature 424 (2003) 657–659.
[3] J.C. Knight, Photonic crystal fibres, Nature 424 (2003) 847–851.
[4] H.-R. Noh, W. Jhe, Atom optics with hollow optical systems, Phys. Reports 372 (2002) 269–317.
[5] J.I. Ramos, Drawing of annular liquid jets at low Reynolds numbers, Comput. Theor. Polymer Sci. 11 (2001) 429–443.
[6] J.I. Ramos, Nonlinear dynamics of hollow, compound jets at low Reynolds numbers, Internat. J. Engrg. Sci. 39 (2001) 1289–1314.
[7] A.D. Fitt, K. Furusawa, T.M. Monro, C.P. Please, Modelling the fabrication of hollow fibers: Capillary drawing, J. Lightwave Technol. 19 (2001) 1924–1931.
[8] A.L. Yarin, P. Gospodinov, V.I. Roussinov, Stability loss and sensitivity in hollow fiber drawing, Phys. Fluids 6 (1994) 1454–1463.
[9] A.D. Fitt, K. Furusawa, T.M. Monro, C.P. Please, D.J. Richardson, The mathematical modelling of capillary drawing for holey fibre manufacture, J. Engrg. Math. 43 (2002) 201–227.
[10] P. Gospodinov, A.L. Yarin, Draw resonance of optical microcapillaries in hollow fiber drawing, Internat. J. Multiphase Flow 23 (1997) 967–976.
[11] S.H.-K. Lee, Y. Jaluria, Simulation of the transport processes in the neck-down region of a furnace drawn optical fiber, Internat. J. Heat Mass Transfer 40 (1997) 843–856.
[12] Z.L. Yin, Y. Jaluria, Thermal transport and flow in high-speed optical fiber drawing, ASME J. Heat Transfer 120 (1998) 916–930.
[13] S.E. Rosenberg, H. Papamichael, I.N. Miaoulis, A 2-dimensional analysis of the viscous problem of a glass preform during the optical-fiber drawing process, Glass Technol. 35 (1994) 260–264.
[14] H. Papamichael, I.N. Miaoulis, Thermal behavior of optical fibers during the cooling stage of the drawing process, J. Materials Res. 6 (1991) 159–167.
[15] H.M. Reeve, A.M. Mescher, Effect of unsteady natural convection on the drawn polymer optical fiber, Optics Express 11 (2003) 1770–1779.
[16] H.M. Reeve, A.M. Mescher, A.F. Emery, Experimental and numerical investigation of polymer preform heating, J. Materials Proc. Manuf. Sci. 9 (2001) 285–301.
[17] R. Siegel, J.R. Howell, Thermal Radiation Heat Transfer, fourth ed., Taylor & Francis, New York, 2002.
[18] S.V. Patankar, Numerical Heat Transfer and Fluid Flow, Hemisphere, Washington, DC, 1980.